Solution-processed light-emitting diodes of monolayers of colloidal quantum wells

a thesis submitted to

the graduate school of engineering and science

of Bilkent university

in partial fulfillment of the requirements for

the degree of

master of science

in

materials science and nanotechnology

By

Hamed Dehghanpour Baruj

June 2022

Solution-processed light-emitting diodes of monolayers of colloidal quantum wells

By Hamed Dehghanpour Baruj

June 2022

We certify that we have read this thesis and that in our opinion it is fully adequate, in scope and in quality, as a thesis for degree of Master of Science

Hilmi Volkan Demir (Advisor)

Dönüş Tuncel

Nihan Kosku Perkgöz

Approved for the Graduation School of Engineering and Science

Ezhan Karaşan

Director of the Graduate School

Abstract

Solution-processed light-emitting diodes of monolayers of colloidal quantum wells

Hamed Dehghanpour Baruj

M.S. in Materials Science and Nanotechnology

Advisor: Hilmi Volkan Demir

June 2022

Semiconductor colloidal quantum wells (CQWs) make an exciting quasi-2D class of nanocrystals thanks to their unique properties emerging from their atomically-flat vertically-thin geometry including highly anisotropic optical transition dipole moment (TDM), giant oscillator strength, and extraordinarily high absorption cross-section. This regular shape of the CQWs enables them to assemble on the surface of a liquid with a high degree of packing, which creates an almost fully uniform monolayer film with the desired orientation. Nearly all of the emission in a single CQW, again because of its geometry, comes from in-plane (IP) transition dipole moments (TDMs). Thus, an assembled film of such CQWs with an all-face-down orientation may show a highly anisotropic and directional emission. Using such a film in an emissive layer (EML) of an electroluminescent device, in this thesis work our intention is therefore to substantially boost photon outcoupling efficiency in a light-emitting device of oriented monolayer of CQWs. Thus far, research efforts have been conducted to investigate the properties of the deposited film of CQWs with self-assembly. However, in all of the previous studies, the property of CQW monolayer has been investigated only in a passive film; therefore, investigation of the self-assembled film in an active device is lacking. In this

thesis, we developed and demonstrated an all-solution-processed colloidal quantum well light-emitting diodes (CQW-LEDs) using a single all-face-down oriented self-assembled monolayer (SAM) film of CQWs that enables a high level of IP TDMs of 92%. This film significantly enhances the outcoupling efficiency of LEDs from 22% (of standard randomly-oriented emitters) to 34% (of face-down oriented emitters). As a result of the outcoupling efficiency increased by 1.55 times, along with the enhanced charge injection and reduced reabsorption in the case of using a single SAM of CQWs, the external quantum efficiency reaches a record high level of 18.1% for the solution-processed type of CQW-LEDs, putting their efficiency performance on par with those of the hybrid organic-inorganic evaporation-based CQW-LEDs and all other best solution-processed LEDs. This EQE value is 65% higher than that in the devices fabricated by spin-coating with the same procedure and structure. Also, the SAM-CQW-LED architecture enables a high maximum brightness of 19,800 cd/m^2 with a long operational lifetime of 247 h at 100 cd/m^2, as well as a stable saturated deep-red emission (651 nm) with a low turn-on voltage of 1.7 eV and a high J_{90} of 99.58 mA/cm^2. These findings indicate the effectiveness of oriented self-assembly of CQWs as electrically-driven emissive layers in improving outcoupling and external quantum efficiencies in the CQW-LEDs.

Keywords

All-solution-processed LEDs, colloidal-LEDs, colloidal quantum wells (CQWs), self-assembly, orientation-controlled film, single monolayer film.

Özet

Koloidal kuantum kuyularının tekli katmanlarını içeren çözelti-bazlı ışık yayan diyotlar

Hamed Dehghanpour Baruj

Malzeme Bilim ve Nanoteknoloji, Yüksek Lisans

Tez Danışmanı: Hilmi Volkan Demir

Haziran 2022

Yarıiletken koloidal kuantum kuyuları, yüksek yönbağımlı optik geçiş dipol momenti, oldukça büyük salınım gücü ve olağanüstü yüksek soğurma kesit yüzeyi dahil olmak üzere atomik olarak düz ve dikey olarak ince geometrilerinden ortaya çıkan benzersiz özellikleri sayesinde dikkat çeken iki boyutlu nanokristaller sınıfını oluşturur. Koloidal kuantum kuyularının düzenli şekli, neredeyse tamamı aynı şekilli ve tek katmanlı bir film oluşturarak yüksek derecede istiflenme özellikleri ile sıvı yüzeyinde bir araya gelmelerini sağlar. Bir koloidal kuantum kuyusunda oluşan ışıma büyük bülümü geometrisinden kaynaklanan düzlem içi geçiş dipol momentleri sayesinde oluşur. Bu nedenle koloidal kuantum kuyularının tamamı aşağı dönük bir yönelimle dizilerek oluşturduğu film, yüksek oranda yönbağımlı ve yönlü bir ışıma gösterir. Bu tez çalışmasında, amaç, yönlendirilmiş koloidal kuantum kuyularını bahsedilen film elektroışıyan katmanında kullanarak ışık yayan aygıtların foton çıkarma verimliliğini arttırmaktır. Bu zamana kadar bu konuda özdizilim üzerıne yapılan araştırmalar koloidal kuantum kuyularından oluşan özdizili film içinde özelliklerini araştırmak üzerinedir. Önceki çalışmaların tümünde koloidal kuantum kuyularının tekli katmanları sadece pasif bir filmde çalışılmıştır, fakat özdizili filmin aktif bir cihaz içinde araştırılması eksiktir. Bu tezde tümü aşağı yönlenmiş olan özdizili ve tek

katmanlı film, ışık yayan diyotlar içinde kullanılmış, %92'ye varan oranda yüzey içi geçiş dipol momenti elde edilmiştir. Bu özdizili film, LED'lerin foton çıkarma verimliliğini önemli ölçüde arttırmış, %22'den (standart rastgele dizilmiş ışıyıcılar için) %34'e kadar (yüzü aşağı yönlendirilmiş ışıyıcılar için) yükseltilmiştir. Arttırılmış yük enjeksiyonu ve azaltılmış yeniden soğurma özelliği ile tek katmanlı koloidal kuantum kuyularından oluşan özdizili filmin foton çıkarma verimi 1.55 kat yükseltilmiştir. Tümü çözeltide gerçekleştirilen ve dış kuantum verimi rekor seviyede %18.1'e ulaşan koloidal kuantum kuyularının kullanıldığı ışık yayan diyotlar, hibrit organik-inorganik buharlaşma temelli koloidal kuantum kuyuları ve diğer yüksek performansa sahip çözelti-temelli ışık yayan diyotlar ile benzer bir verimliliğine çıkmıştır. Dış kuantum verimliliği %65 ile, aynı prosedür ve benzer bir yapı ile döndürülerek kaplanmış aygıtlardan daha yüksektir. Ayrıca, tek katmanlı özdizili koloidal kuantum kuyularının kullanıldığı aygıt, 100 cd/$m^{2'}$ ışıldama seviyesinde 247 saatlik uzun çalışma ömrüyle 19.800 cd/m^2 maksimum parlaklığa ulaşmıştır. 1.7 eV'luk düşük çalışma voltajı ve 99.58 mA/cm^2'lik yüksek akım yoğunluğuna sahip olan aygıt, kararlı ve aşırı doygun kırmızı ışıma göstermektedir. Bu çıktılar, yönlenmiş ve özdizili koloidal kuantum kuyularının elektrikle çalışan ışıyıcı katmanlarda kullanılması, foton çıkarımı ve dış kuantum verimliliklerini iyileştirmedeki etkinliğini göstermektedir.

Anahtar kelimeler

Çözelti-temelli ışık yayan diyotlar, koloidal ışık yayan diyotlar, kuantum kuyuları, yönlendirilmiş koloidal kuantum kuyuları, tek katmanlı film.

Acknowledgment

I would like to present my appreciation to Prof. Hilmi Volkan Demir for his guidance and support through my thesis work.

I would also want to thanks my jury members Prof. Dönüş Tuncel and Prof. Nihan Kosku Perkgöz for their for their time to read and evaluate my thesis and providing their invaluable feedback

I am also grateful for the members of Hilmi Volkan Demir group for their helpful and friendly environment.

My deepest thank is for my dearest friend Farzan, who helped me to join the Demir Group and support me in everything.

It is my great pleasure to thank to whole LED team: Dr. Betül Canımkurbey, Iklim Yurdakul, Ilayda Özkan, and Ahmet Tarık Işık. I never forgot the moment when we saw a working device with Betul and Iklim. Also, I will not forget the days we had in cleanroom using the glove-box system. To be honest, finishing of this project could not be possible without their deep love and help.

Also, I would like to give my thanks to the whole Demir group members, Özgün Akyuz, Emre Ünal, Dr. Savaş Delikanlı, Furkan İşik, Rabia Onen, Ebru Ercel, Dr. Volodymyr Sheremet, Dr. Nina Sheremet, Dr. Zeynep Dikmen, Dr. Satish Kumar, Sina Foroutan-Barenji, Taylan Bozkaya, Taha Haddadifam, Rumon Miah, Muhammad Ahmad, Tuğba Karahan, Anıl Çağrı Atak, Mohsin Waris, Tevfik Bülent Kanmaz.

Finally, I desire to express my deepest love to my lovely mother, Mahboubeh, my father, Mohammad Taghi, my brother, Hadi, and my sister, Nasrin, for all the loves and support they have provided me with through these years.

CONTENTS

List of Figures

Chapter 1

INTRODUCTION

As a practical thin-film deposition technique, oriented self-assembly of the colloidal two-dimensional nanocrystals (NCs) allows for controlling the orientation. This method leads to the formation of a highly uniform, pinhole-free, single monolayer nanocrystal film with a well-defined orientation over several tens of centimeter squares [1], [2], [11]–[16], [3]–[10]. This approach also enables us to take advantage of the inherent direction-dependent properties of colloidal nanocrystals originating from their shape and electron confinement behavior. Thus far, the successful creation of a highly uniform, pinhole-free, all face-down or edge-up films from such two-dimensional nanocrystals has been reported, and their properties have been investigated thoroughly [17], [18]. However, in all of the previous studies, the investigation was carried out in a passive thin film, where the structures are excited optically using an external light source. Consequently, the properties of such an oriented film of nanocrystals in an active device platform have remained unexplored.

Semiconductor colloidal quantum wells (CQWs), alternatively nicknamed nanoplatelets (NPLs), having a quasi-two-dimensional structure with well-defined vertical thickness, have emerged as an important class of NCs [19]–[22]. Compared to their spherical counterparts, NPLs exhibit a narrow emission bandwidth because of their suppressed inhomogeneous broadening, extraordinary large absorption cross-section owing to their giant oscillator strength [23], highly suppressed Auger recombination thanks to their non-confined lateral dimensions, and highly anisotropic transition dipole moments (TDMs) thanks to their one-dimensional strong electron confinement [11], [12], [30]–[33], [21], [22], [24]–[29]. These features have led to the fabrication of high external quantum efficiency (EQE) and high-color purity colloidal quantum well light-emitting diodes (CQW-LEDs) using hybrid organic-inorganic device structures. For example, in a previous work of our group, we reported a high EQE value of 19.2% with a maximum brightness of 23,490 cd/m^2 for the hybrid organic-inorganic inverted CQW-LEDs [10]. However, the efficiency of CQW-LEDs having only all-solution processed structures in their layers is still lagging far behind the state-of-the-art values obtained with evaporation-based devices [28], [34], [35]. Since this architecture is relatively easier to fabricate and cheaper than evaporation-based ones, achieving a high EQE from all-solution-processed LEDs is of great interest. Thus far, Kelestemur *et al*. reported the highest EQE of 9.92% with a maximum brightness level of 46,000 cd/m^2 for all-solution processed red CQW-LED [28]. However, this EQE value was insufficient to fulfill the high level industrial demands. The fundamental light-extraction efficiency limitation and exciton quenching of the zinc oxide (ZnO) layer impede the maximum EQEs from

reaching the state-of-the-art values in the case of all-solution processing [10], [16].

As a new strategy, we target to overcome the light extraction efficiency limitation by exploiting self-assembled monolayer (SAM) films of NPLs as an emissive layer (EML) [36]–[38]. In this regard, NPLs are highly advantageous owing to their anisotropic TDMs [36]–[38]. The CQWs are from the family of anisotropic nano-emitters that exhibit almost all in-plane (IP) TDMs [30], [37]–[42]. Thus, an all-face-down ensemble film of CQWs can act as a highly anisotropic EML. The Fresnel equation suggests that, from the emitter's point of view, the ray escape cone has an opening angle of 30° to the surface normal [30], [37]–[39]. Accordingly, the density of light inside the cone determines the intensity of extracted light. It has been reported that the ratio of optical power inside the cone is higher in a device with directional EML than that in the isotropic EML [30], [37], [38], [40]–[46].

In addition, self-assembly provides the lowest possible root-mean-square (RMS) roughness among the various deposition techniques yielding an RMS roughness level comparable with that of the spherical nanocrystals [10], [47]. The film roughness, especially the EML film roughness, is a deterministic factor in the efficiency of the devices [10], [15], [26], [48], [49]. It is known that the interlayer transfer of electrons occurs by the hopping process, which depends on the atomic-scale distance between layers and hence the roughness of EML [20], [50]. Thus, self-assembled NPLs as an EML provide unique advantages.

In this thesis, we proposed and demonstrated a high-performance all-solution-processed CQW-LED having all-face-down SAM film of NPLs as an

EML through precise control of their orientation in the liquid-air self-assembly for the first time. Our optimized device architecture is made of consecutive layers of indium tin oxide (ITO, 100nm)/poly(ethylene dioxythiophene):polystyrene sulphonate (PEDOT:PSS, 30nm)/poly (N,N9-bis(4-butyl phenyl)-N,N9-bis(phenyl)-benzidine) (p-TPD, 20nm)/poly(9-vinyl carbazole) (PVK ,10nm)/NPLs/$Zn_{0.95}Mg_{0.05}O$(30nm)/Al(100nm). Applying back-focal plane (BFP) imaging techniques on our all-face-down SAM film of NPLs, we measured TDMs direction (Θ) to be 92% in-plane (IP). Considering our device's structure, we calculated the outcoupling efficiency to be 34%, which is significantly higher than 22% of the conventional solution-processed structures with isotropic emitters as an EML and without any light extraction feature. Our SAM-CQW-LEDs reached an outstanding EQE of 18.1 along with a high luminance level of 19,800 cd/m^2 and a long lifetime of 247h at 100 cd/m^2 using ligand-exchanged CdSe/$Cd_{0.25}Zn_{0.75}S$ core/hot-injection shell (HIS) NPLs. These values are comparable to those of the best reported organic-inorganic hybrid CQW-LEDs, state-of-the-art OLEDs, PeLEDs, and QLEDs. In this work, we have, therefore, addressed the fundamental outcoupling efficiency limitations commonly encountered in conventional colloidal device structures.

Chapter 2

SCIENTIFIC BACKGROUND

2.1 Quantum confinement effect

The size-dependent bandgap energy variation of the semiconductor nanocrystals (NCs) is known as the quantum confinement effect. The mathematical expression of this phenomenon can be obtained through the solution of the Schrödinger equation (Eq. 2.1) using the particle-in-a-box model. The solution gives in energy eigenvalues (E_n) (Eq. 2.2) that depend on the box's size (see Figure 2.1). The eigenenergy value increases by narrowing down the box's size (L). Here, E_n represents the electronic state's energy values.

$$-\frac{h^2}{2m}\frac{d^2\psi(x)}{dx^2} = E\psi \qquad \text{(Eq. 2.1)}$$

$$\mathrm{E_n} = \frac{h^2 n^2}{8mL^2} \qquad \text{(Eq. 2.2)}$$

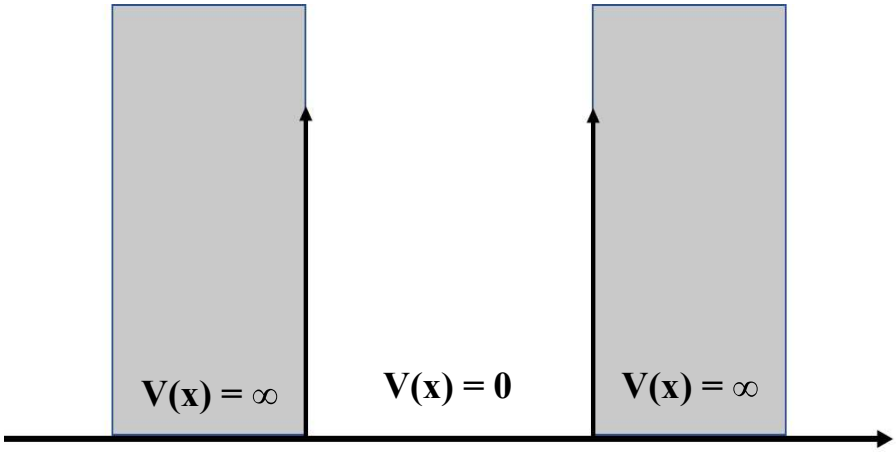

Figure 2.1: *Schematics of the particle in a box with a potential energy of each region.*

Optical emission in semiconductor originates from a vertical downward transition from the first excitonic state the ground state. Therefore, a decrease in the size of the NC shifts the emission toward the shorter wavelengths. This confinement effect is more pronounced when the size the nanocrystal becomes comparable with the exciton Bohr radius. As shown in Figure 2.2, an increase in the size of NC decreases the bandgap energy and the wavelength of emitted light shift to a longer wavelength.

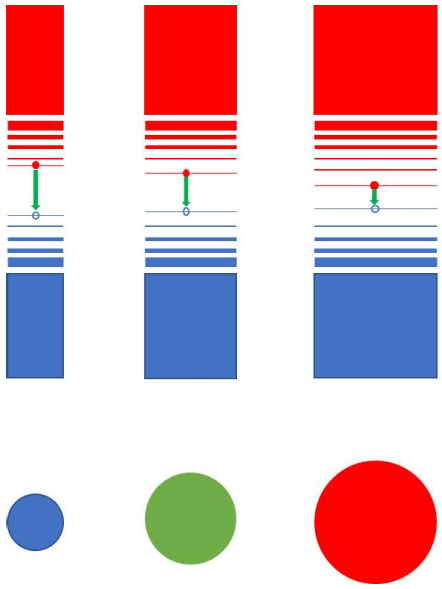

Figure 2.2: *Schematics of the dependence of bandgap energy on the size of nanocrystals.*

The exciton Bohr radius describes the distance between an excited electron and its hole, which, in the case of CdSe NCs, is 5.6 nm. In NCs, depending on the dimension that have a size comparable to the exciton Bohr radius, a different dimensions of confinement are possible: one, two or three-dimensional (1D, 2D, 3D). If only one dimension (thickness) of an NC is comparable with the exciton Bohr radius such as in the nanoplatelets (NPLs), this NC experiences a 1D confinement effect. If the two dimensions (thickness and width) are in that range, this NC feels a 2D confinement, such as in the nanorod. Finally, if all three dimensionsof an NC are comparable with the exciton Bohr radius, such as it is subjected to a 3D confinement effect, in the quantum dots (QDs).

2.2 Colloidal quantum wells (CQWs)

This section provides general information about the CQWs and their heterostructures, ligand-exchange process, and self-assembly.

2.2.1 CQWs heterostructures

The lateral sizes of NPLs are in the range of 10-50 nm, significantly larger than the exciton Bohr radius, which is in the range of several nanometers. Ithurria *et al.* [22] has discovered the method for synthesizing CdSe core NPLs in reproducable way. Thus far, a lot of research has been devoted to exploring NPLs' properties. The previous reports demonstrated the formation of 4.5 and 5.5 monolayers (MLs) consisting of alternating Cd and Se layers (see Figures 2.3 a-b). Notably, the two facets of an NPL terminated by (100) plane of Cd atoms;

therefore, one extra Cd layer always exists. For example, in the 4.5 ML, there are four atomic layers of Se and five atomic layers of Cd.

A typical emission and absorption spectra of 4.5 ML and 5.5 ML NPLs are given in Figures 2.3 a-b. In this figure, the low-energy excitonic peak (for example, 512 nm in 4.5 ML) is the heavy-hole (hh) peak and the second one (490 nm in 4.5 ML) is the light-hole (lh) (see Figure 2.3a). These two peaks are the characteristic excitonic peaks for NPLs rooted in a split in conduction band offsets. Their absorption profile is similar to epitaxial growth quantum wells; both have a stepwise density of states (DOS). In addition, compared to their spherical counterparts (quantum dots), NPLs exhibit a narrow emission bandwidth due to their suppressed inhomogeneous broadening. Typically, the full-width-half-maximum (FWHM) of the NPLs is in the range of 7-11 nm.

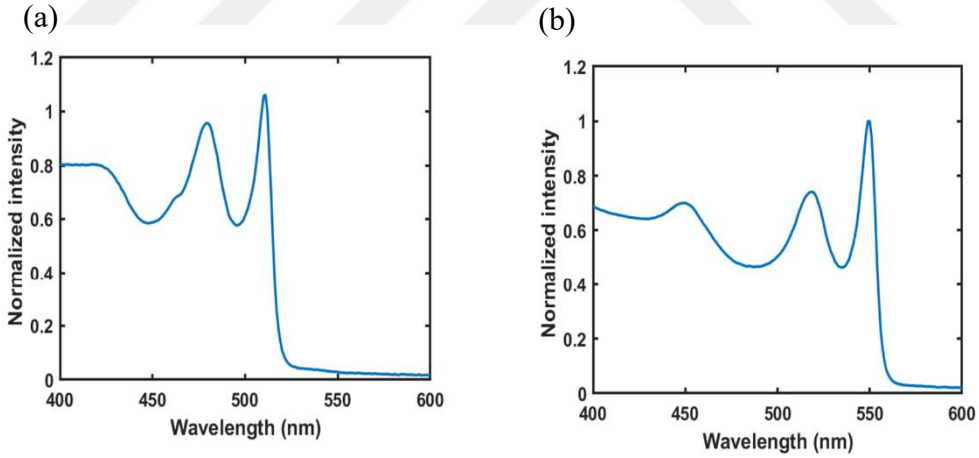

Figure 2.3: Photoluminescence (PL) and absorption spectra of a) 4.5 and b) 5.5 monolayer CdSe CQWs.

In addition, the NPLs possess an extraordinarily large absorption cross-section owing to their giant oscillator strength and highly suppressed Auger recombination thanks to their non-confined lateral dimensions. These properties make these materials an excellent candidate for light-emitting diodes (LEDs) and

colloidal lasers. However, the cores may suffer from low photoluminescence quantum yield (PLQY) due to nonradiative recombination sites on the surface originating from unpassivated dangling bonds.

To passivate the surface of the NPLs, different heterostructures of core/shell, core/crown, and their combinations have been introduced thus far. Considering the various heterostructures, the core/shell architecture shows a higher PLQY than the core/crown structure; it could more effectively passivate the surface of NPLs. Therefore, coating a shell on the core could be the most effective method for passivating the surface, which improves the PLQY. The shell usually consists of several monolayers of wide-bandgap inorganic semiconductors such as ZnS, CdZnS, and CdS surrounding the core. Since coating increases the thickness of NPLs, this relaxes the confinement. Thus, the emission red-shifts after growing a shell. The common methods for growing a shell on the core are atomic layer deposition (c-ALD) and hot injection (HIS).

Colloidal atomic layer deposition (c-ALD) is a layer-by-layer growth method in which the various monolayers of atoms are sequentially added up on top of each other to make a layered shell for an NC [28], [51], [52]. The c-ALD is usually carried out at room temperature and offers a very precise control over the number of monolayers. However, this technique usually yields low PLQY and low stability due to the nature of the synthesis process. Thus far, there are a few reports on enhancing the photophysical properties of core/shell NPLs using the c-ALD method. Delikanli *et al.* [11], [53] have reported high PLQY NPLs of CdSe/CdS@$Cd_xZn_{1-x}S$ core/crown@gradient-alloyed shell CQWs using the c-

ALD method. They have demonstrated an ultralow amplified spontaneous emission (ASE) threshold in the solution.

The other method for growing a shell on the core is the hot-injection method or HIS method [54]. This technique has been introduced for growing a shell on colloidal quantum dots (CQD) since the early 90's, enabling a uniform distribution of NCs with a high PLQY. In this method, the cation precursors have been added at room temperature, followed by continuously injecting the anion precursor at higher temperatures. The Norris group reported using this method for growing shells on CQWs [55]. They successfully coated the CdS shell on CdSe cores. The acquired NPLs exhibited a maximum PLQY of 60%. Since the shell of CdS has a low lattice mismatch with the CdSe core due to the vicinity of the conduction band between both core and shell materials, the electron wavefunction delocalizes to the shell. This increases the nonradiative Auger recombination and sensitivity to the surrounding dielectric media. The Demir group introduced the ZnS shell, which significantly enhances the PLQY and stability of core/shell NPLs [56]. However, the shell of ZnS causes a considerable lattice mismatch between the core and shell, limiting the PLQY from reaching very high values. Thus, a combination of these two materials in the form of a graded shell (CdSe/CdZnS) has been introduced as a high-quality shell structure, which shows an outstanding PLQY of 95% in solution with high stability [54]. The graded structure of this shell enables a low lattice mismatch between the core and the shell, which significantly reduces the nonradiative recombination. Also, the carriers see a lower energy potential in moving from the shell into the core region and reverse. Figure 2.4 shows the band offset of the core and various shells where the bandgap energy of both shells are higher than that of the core.

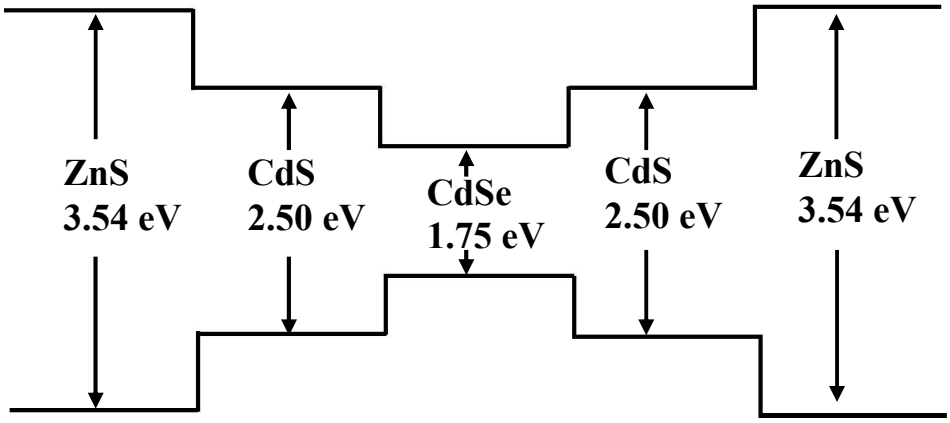

Figure 2.4: *Schematics of bandgap structure of CdSe core with CdS and ZnS shells.*

2.2.2 CQWs ligand-exchange

A polymeric or inorganic surfactant, called a ligand, is used for passivating the surface traps of NCs and enabling solubility in a solvent. The commonly used ligands during the synthesis process for CQWs are oleic acid (OA) and oleylamine (OLA). Figure 2.5 shows the chemical structure of these ligands. They have a large organic chain (eighteen carbons) with a functional group attached to one end. Also, these ligands have nonpolar properties, making the synthesized NC soluble in the nonpolar solvents.

(a)

(b)

Figure 2.5: *Chemical structure of a) oleylamine and b) oleic acid.*

The ligands added to the NPLs during the synthesis process are the as-synthesis ligands. Usually, these ligands' long-organic tail affects the charge or energy transfer efficiency from or into the NPLs by enlarging the hopping or transfer distance, limiting their performances in optoelectronic applications.

The concept of ligand exchange has been introduced to modify the physical and electrical properties of NCs [20], [50]. The ligand-exchange process is replacing the as-synthesis ligands with other organic or inorganic ligands to change their physical and chemical properties. The replacement of ligands could be undertaken for several reasons. For example, shorter ligands modify the hopping length in the CQWs, facilitating the charge hopping in their ensemble film. Also, since the ligand's nature (polarity) determines the solvent (polar or nonpolar) for NCs, the ligand exchange can be a way to change the solvent type. For example, the as-synthesized NPLs with OA or OLA ligands dissolve in nonpolar solvents such as hexane. But changing these ligands by phenylpropanolamine (PPA), the NCs can be soluble in polar solvents such as water. In addition, ligand exchange enables us to use both the organic such as amine-based or thiol-based organic ligands (for example, 2-Ethylhexanethiol (EHT) (Figure 2.6)), or inorganic, such as alkali metal sulfides, amide, hydroxides, and hydrogen sulfide ligands [49], [57].

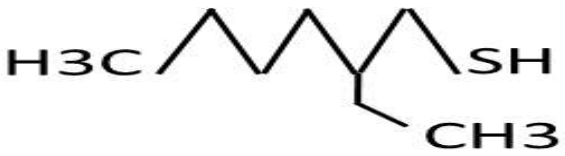

Figure 2.6: *Chemical structure of 2-Ethylhexanethiol (EHT) ligand.*

The ligand exchange process can be performed in solution or film after depositing. In the solution form, the as-synthesized NPLs, in a controlled environment, mixed with the ligands' solution, kept for some duration and washed. In the in-film method, a substrate containing a deposited film of the as-synthesized NPLs has been exposed to the ligand solution and then rinsed with cleaning solvents.

2.2.3 CQWs self-assembly

The spontaneous ordering of separate components into ordered structures is called self-assembly. At the first stage of the process, the individual particles have a collectively random movement until they come together in an organized structure. The order of such a structure is obtained by the interaction between the particles and the media. The technical details of this method vary with on the material type and the medium.

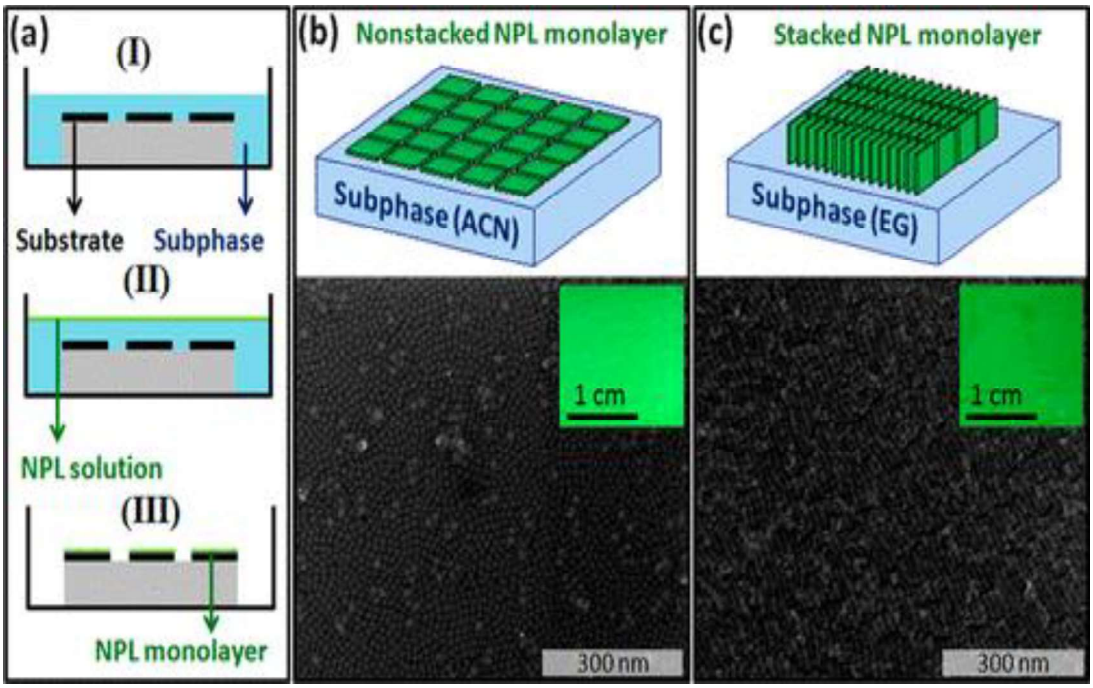

Figure 2.7: *a) Schematic illustration of liquid-air self-assembly starting with (I) substrates and subphase and contenuing with (II) NPLs solution and (III) draining. b) Sketch of face-down*

oriented CQWs with its scanning electron microscopy image. c) Sketch of edge-up oriented CQWs with its scanning electron microscopy image. With permission from ref. [58]. *Copyright © 2019, American Chemical Society.*

To control the orientation of CQWs, various approaches of solvent destabilization [2], drying mediate [59], doctor blade [60], and liquid-air self-assembly have been introduced [17]. Among them, the liquid-air self-assembly method is the most suitable method for controlling the orientation of NPLs over a large area, creating a highly uniform film. In this process, NPL solution is introduced to the surface of an immiscible solvent with the solvent of NPLs to create a monolayer film on the liquid surface, followed by a transfer process. Here, the subphase cannot dissolve the organic ligands capped NPLs, creating a surface for spreading the NPLs across the surface. The transferring process has been carried out after full evaporation of the solvent of the NPLs in which a thin membrane of CQWs remains sitting on a desired substrate. Usually, the transfer of the film is carrying out by draining the solvent from the bottom of the container in which self-assembly process taken place.

Usually, both directions of face-down (the large facet orienting parallel to the surface of the substrate) and edge-up (the large facet orienting perpendicular to the surface of the substrate) (see Figures 2.7 b-c) can be obtained in the liquid-air self-assembly. Here, the interaction force between the subphase polar solvent (ethylene-glycol, diethylene-glycol, acetonitrile, etc.) [57], [61] and the NPLs' nonpolar solvent (hexane, octane, etc.) determines the direction of the NPLs; the higher difference in the polarity of solutions results in the edge-up configuration and the lower difference results in the face-down. Scanning electron microscopy (SEM) images of the face-down and edge-up films are presented in Figure 2.7. In

most of the cases, for obtaining the face-down orientation of CQWs in hexane or octane solvents, the diethylene-glycol (DEG) and for the edge-up configuration, ethylene glycol (EG) are used as a subphase. Here, the polarity of EG is higher than that in the DEG; therefore, it imposes higher forces on the CQWs, which leads to the edge-up configuration.

The second deterministic factor for controlling the orientation of CQWs is their solvent's nature. It has been reported that the evaporation rate of the solvent could affect the orientation of CQWs by giving more time for NPLs (low evaporation rate), they tend to stand in edge-up configuration[41]. Accordingly, the solvents with a higher evaporation rate favor face-down configuration. For example, self-assembly of CQWs in the octane solvent is more likely to create the edge-up configuration film, whereas NPLs in hexane align face-down [38], [41]. In this regard, many different strategies have been developed for controlling the evaporation rate of solvent and achieving the desired CQWs configuration, such as using different solvents or controlling the vapor pressure of the solvent in the self-assembly vessel.

2.3 Light-emitting diodes (LEDs)

CQWs offer promising performance levels in light-emitting diodes. In this section, we are explaining the principles of their LED device and its related parts of the device.

2.3.1 Working principles

A light-emitting diode is an optoelectronic device that emits light when an electric current passes through its structure. The first demonstrated LED device was by

Oleg Losev in 1927 [62]. In the simplest form, an LED consists of a layer of emissive semiconductor material sandwiched between two electrodes deposited on a substrate, usually glass or quartz. During the operation, an electrical potential is applied across the electrodes in direct current (DC) mode in a way that the holes are injected from the anode (the positive electrode) and the electrons, from the cathode (the negative electrode). Finally, both the injected electrons and holes recombine in the emissive semiconductor layer and generate a photon.

In the surface-emitting planar LEDs, one of the electrodes must be transparent to allow the generated light to be outcoupled. Also, it must also provide good electrical conductivity, chemical stability, and mechanical properties. The most popular and practical type of transparent electrode is made of indium tin oxide (ITO) deposited on a glass substrate [15], [48], [63]–[65].

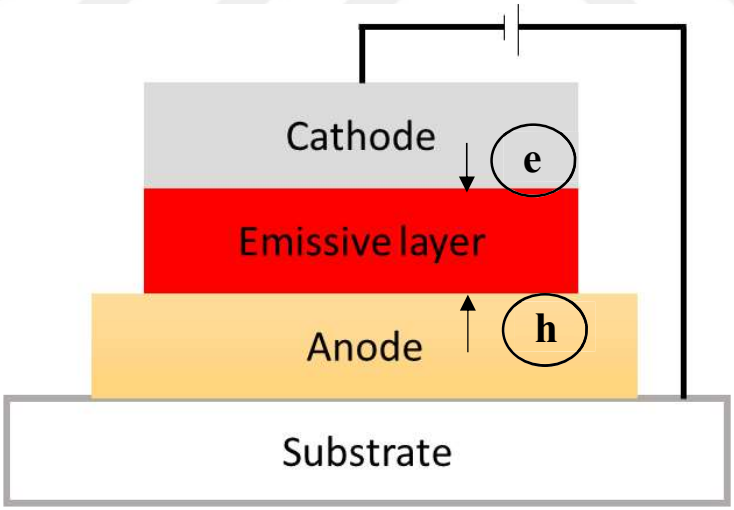

Figure 2.8: *Schematic illustration of the simplest architecture of a LED.*

While flowing the current of electrons through the device from cathode to anode, as is shown schematically in Figure 2.8, electrons enter the conduction band (CB) or the lowest unoccupied molecular orbital (LUMO), and the holes into the valance band (VB) or the highest unoccupied molecular orbital (HOMO)

of the emissive layer (EML). Here, the electrostatic forces between holes and electrons bring them together to form an exciton (electron-hole pair) in the EML. The recombination of electrons with holes results in downward transition electrons. This relaxation of energy states produces light at a specific wavelength depending on the band-gap energy of the EML material.

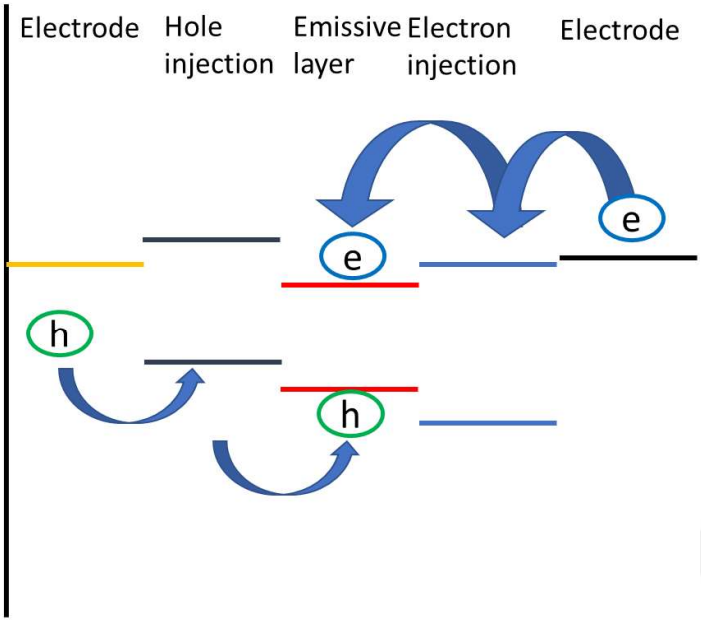

Figure 2.9: *Schematic illustration of electron and hole movement in the LEDs.*

The magnitude of the released energy is equal to the energy of the effective bandgap of the semiconductor (E_g), which is the difference between conduction band minimum (E_c) and valance band maximum (E_v) with Coulomb interaction corrections [66]. Resultantly, the EML's bandgap energy (E_g) determines the color of emitted light based on the relation of electromagnetic wave frequency to the photon energy ($E = h\nu$). In this equation, E is the bandgap energy, h is Planck's constant, and ν is the frequency of light.

2.3.2 LED architecture

The aforementioned structure is the simplest form of planar LEDs, which consists of three primary layers. However, this type of structure cannot efficiently carry the electrons and holes to the EML for recombination because it presents a considerable energy barrier for charge movements, which causes malfunctioning of the device or reduction in device performance. Therefore, the engineered layered architectures have been introduced to facilitate the charge movement from electrodes to the EML; such a structure presents a gradual and stepwise energy profile. It also blocks the carriers from reaching the other electrode to be wasted. As shown in Figure 2.9, the holes and electrons can easily move through a step-like energy band from electrodes to the EML with facing a low energy barrier. In this regard, the different intermediate layers of organic or inorganic semiconductors have been introduced [66]. The standard form includes a hole injection layer (HIL), a hole transport layer (HTL), an electron injection layer (EIL), and an electron transport layer (ETL) (see Figure 2.10).

2.3.2.1 *Electrodes*

Electrodes are metallic or conductive compound materials in direct contact with the power sources. Transparent indium tin oxide (ITO) is the commonly used substance as an electrode in the LEDs for either cathode or anode side typically with a thickness of 100-150 nm. It is highly transparent with reasonably good levels of hole and electron mobility and conductivity. It also provides a suitable work function, in the range of 4.60 – 4.75 eV. This range eases the hole injection into the LED by generating a relatively low energy barrier for holes to enter the VB of HOMO levels of HIL. As opaque electrodes, aluminum, silver, chromium,

and gold are the commonly used layer in planar LEDs. Their thickness is typically in the range of 80-150 nm, which presents sufficient enough conductivity.

2.3.2.2 Hole injection layer (HIL)

The hole injection layer is a p-type semiconductor –the material with excess holes in its structure– placed in contact with the electrode. Usually, the highest occupied molecular orbital (HOMO) or valance band maximum (VBM) level of these semiconductors is close to the Fermi level of the metal electrode to provide a small energy barrier for holes to move from the electrode to this layer. The HIL could be an organic material such as poly(3,4-ethylene dioxythiophene): polystyrene sulfonate (PEDOT: PSS) [14], [67], or it can be inorganic such as molybdenum oxide (MoO_3) [10]. The hole mobility in this layer should also be high enough to transfer holes to the next layer.

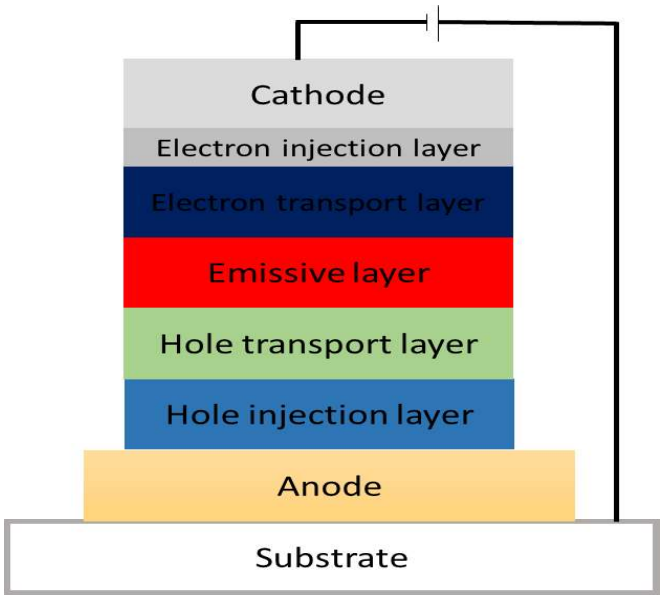

Figure 2.10: *Sketch of various layers of a planar LED.*

2.3.2.3 Hole transport layer (HTL)

HTL is an intermediate layer between the EML and the HIL (see Figure 2.10). HTL consists of a layer of semiconductor material with a HOMO or VBM energy level between the HIL and EML (see Figure 2.9); the primary goal of this layer is to decrease the energy barrier for holes to move from the HIL to the EML. This layer could be either organic or inorganic semiconductor material. In some cases, to decrease the energy barrier of charge movement, multiple-HTL has been used. For example, Lei et al. [68] used co-HTL of PVK and p-TPD to create a stepwise band-energy alignment to facilitate the charge injection.

2.3.2.4 Electron injection layer (EIL)

An EIL is a layer of n-type –the material with excess electrons in its structure– semiconductor material in direct contact with the anode electrode. This layer should provide good electron conductivity and mobility, injecting the electrons inside the LED. This layer's conduction band minimum (CBM) or LUMO energy level is close to the Fermi level of the electrode material. As a result, the electrons can easily make it to this layer to diffuse further inside the structure. This layer could be either fully an organic material with an engineered structure or fully an inorganic semiconductor. One widely used semiconductor for EIL is a thin layer of lithium fluoride (LiF) [47].

2.3.2.5 Electron transport layer (ETL)

An electron transport layer consists of a layer of n-type semiconductor, either organic or inorganic, with a CBM or LUMO level between the HIL and EML. This layer act as an intermediate layer for decreasing the energy barrier for

movement of the electrons. Usually, the ETL is thicker than the EIL. An example of the ETL is the 4,4′-Bis(N-carbazolyl)-1,1′-biphenyl (CBP) [53] polymer, which is processed in solution and spin-coating or evaporated as a film.

2.3.2.6 Emissive layer (EML)

EML is the layer of a direct bandgap semiconductor where an electron recombines with a hole to produce a photon, which depends on the material's effective energy bandgap (E_g). The type of LED may be categorized in accordance with the nature of this layer; for example, if the EML's material is organic, it is called organic LED or (OLED) [69]. For quantum dots, it is QLED [49]; for perovskite it is Pero-LED [4], and for colloidal quantum wells, it is CQW-LED [53]. This layer must present special properties such as high in-film PLQY, high film uniformity, high optical and chemical stability, and low density defects [66].

2.3.3 LED categorization and types

Standard LEDs are categorized based on the EML material, the substrate's mechanical property, the architecture, and the fabrication methods.

2.3.3.1 LED types based on architecture

Based on LED architecture, two types of devices exist: the normal and the inverted structures. In the normal architecture, the light outcouples from the hole-injection electrode or anode side (see Figure 2.11a). In this type, the ITO is widely used as a transparent hole-side electrode. This structure is suitable for all types of materials with various deposition methods. The inverted structure LEDs are the ones where the light is out-coupled from the electron injection electrode or

cathode. These two types of LEDs have been shown schematically in Figure 2.11b.

2.3.3.2 LED types based on the fabrication method

Another way of categorization of LEDs is the fabrication method. Here two primary techniques for fabricating an LED are in-solution or evaporation-based depositions. However, some LEDs have been manufactured using a combination of both methods.

2.3.3.2.1 Solution based methods

The solution-processed method is a thin-film deposition technique that uses a spinner to deposit a target material, which is in liquid phase, onto a substrate. In this process, a small amount of target material in the form of a solution is added to the center of a substrate while rotating or in static mode. Then, the substrate rotates at a prescribed speed (up to 10,000 rpm) to spread the material by centrifugal forces.

In this process, the thickness of the deposited film is controlled by the solvent's concentration, viscosity, and rotation speed of the spinner. Increase in the solvent concentration or decrease in the rotation rate increase the film's thickness. As this method does not require costly instruments such as high-vacuum chambers, it is a widely used technique for device fabrication. It enables the fabrication of affordable and reproducible optoelectronic devices.

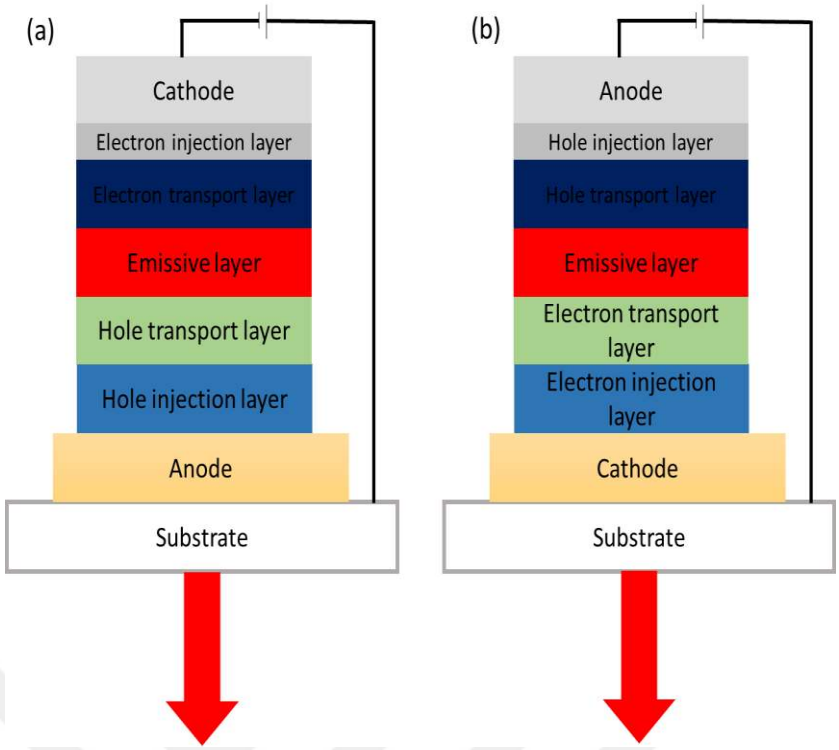

Figure 2.11: *Schematical illustration of a) normal architecture and b) inverted structure of planar LEDs.*

2.3.3.2.2 Evaporation based methods

Deposition of the vapor of a material on to a substrate is called evaporation-based deposition. This method requires ultra-high vacuum chambers and very precise controllers. In this process, the substrate is placed on top of a boat containing the target material (organic or inorganic), which is heated to evaporation temperature. Under ultra-high vacuum, the target material's vapor reaches the substrate, creating a highly uniform thin film. In the case of LED fabrication, the thermal evaporator system is usually attached to a glove box system to operate in an oxygen-free medium.

2.3.4 Properties of LEDs

To analyze the performance of LEDs, several methods have been introduced. Here, we summarize the characterization analysis tools which we used in our work.

2.3.4.1 Luminance

Luminance quantifies the light intensity or brightness per unit area in a given direction. It is used to quantify the emission or reflection from a surface, indicating the brightness of a given surface. The international system of units (SI) of luminance is candela per square meter (cd/m^2). In this unit, 1 candela is approximately the amount of light that comes from one candle from a one meter distance.

2.3.4.2 International Commission on Illumination (CIE) coordinates

The International Commission on Illumination (CIE) coordinates relate the wavelength distribution of the electromagnetic spectrum to the color that human vision can detect. Figure 2.12 shows the typical CIE diagram with three edges representing red, green, and blue colors. The diagram is placed on a cartesian axis of x and y. Each (x,y) value represents a color point in the graph, which shows the perceived color of that point. Based on these x and y values, the color of the emitted light could be identified.

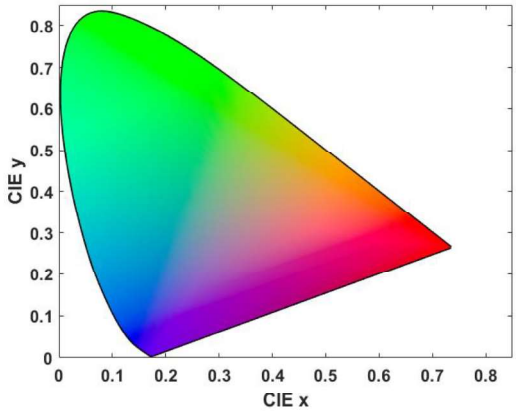

Figure 2.12: *Color diagrams of the International Commission on Illumination (CIE).*

2.3.4.3 Current density voltage (J-V)

The current density voltage diagram of LEDs is a graphical representation of the non-linear dependence of current density flowing through a device in response to the applied voltage across it. Figure 2-13 shows a typical behavior of the J-V diagram of a CQW-LED. In this diagram, the current density increases rapidly in response to a slight increase in the voltage, after a specific voltage known as the turn-on voltage. Noteworthy, the turn-on voltage is commonly taken as the voltage value corresponding to the current density of 1 mA/cm^2. Graphically, it is the intersection of the linear part of the diagram with respect to the voltage axis. Followed by the linear region, the graph reaches a plateau where the current density does not change while increasing the voltage, which is the saturation region. Finally, the diagram comes down to a point where the device starts to fail possibly by overheating (see Figure 2.13).

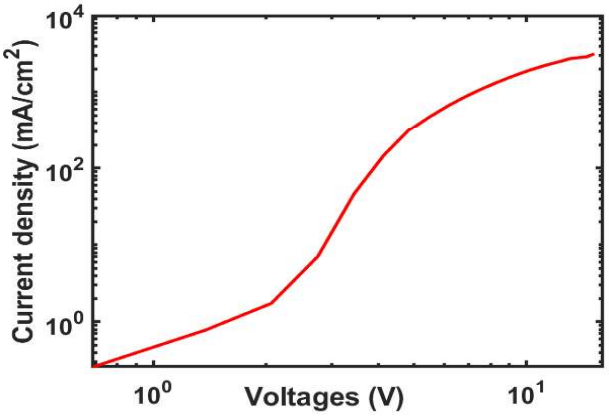

Figure 2.13: *A typical J-V behavior of a CQW-LED.*

2.3.4.4 Lifetime

The lifetime of a LED is defined as the time it takes for it to reach half of the initial brightness, commonly taken at the initial luminescence of 100 cd/m^2, shown by T_{50}. Usually, reaching to T_{50} in the 100 cd/m^2 brightness takes too long. Therefore, to ease the measurement, the test is performed at a higher initial brightness (for example, 5000 cd/m^2), and then using the relation of $L_0{}^nT_{50} = L_1{}^nT$, the T_{50} for the illumination of L_1= 100 cd/m^2 is being calculated. Here, L_0 represents the initial test brightness, T_{50} is the half-life time for the brightness of L_0 measured during the test, and n is the acceleration factor, typically taken as 1.5 for the case of CQWs [10]. This metric depends on many factors such as the stability of EML material, the device architecture, the charge transport layers' stability, and the charge accumulation in the device.

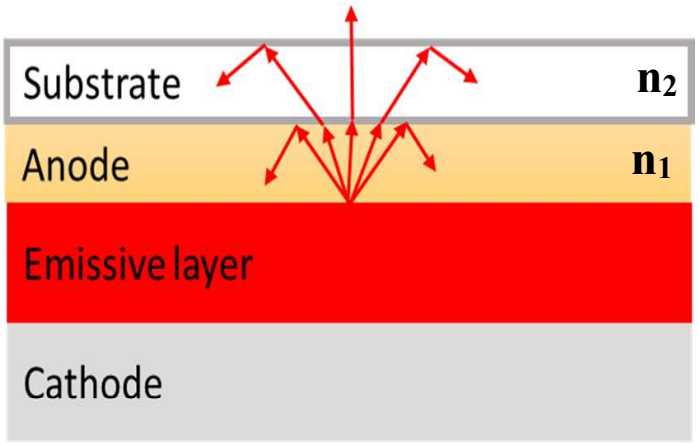

Figure 2.14: *Schematic illustration of the ray path inside a LED structure.*

2.3.4.5 Efficiency

For measuring the performance of LEDs, several efficiency definitions have been introduced. Among the important ones are external quantum efficiency (EQE) and light-extraction efficiency.

2.3.4.5.1 External quantum efficiency (EQE)

EQE is the most critical metric for measuring the performance of a LED. EQE is defined as the ratio of the number of outcoupled photons to the number of injected electrons. Also, it can be calculated theoretically using the relation for internal quantum efficiency (IQE) in Eq. 2.3:

$$IQE = r.q.\gamma \qquad \text{Eq. 2.3}$$

$$EQE = \eta_{out}.IQE \qquad \text{Eq. 2.4}$$

In Eq. 2.4, η_{out} represents the photon extraction efficiency or outcoupling efficiency,and in Eq. 2.3 r represents the fraction of excitons with the probability of radiative recombination, q is the film PLQY, and γ represents the charge

injection efficiency inside the device. Higher PLQY, balanced electron-hole injection, and better outcoupling efficiency lead to a better higher efficiency.

2.3.4.5.2 Light extraction efficiency (η_{out})

Fresnel equation proves that a large portion of produced light in the EML can not escape from the LED's structure (see Figure 2.14). This happens because the total internal reflection occurs at the interface of glass and air due to a difference in the refractive indices. To overcome this issue, some smart designs have been introduced to improve the $\eta_{out,}$ including the patterned glasses, the curved glasses, and directional EML. The former ones are applicable to almost any type of LED. However, the last one is just for particular materials which possess a directional emission.

Directionality in emission could be utilized in order to improve the outcoupling efficiency. As shown schematically in Figure 2.14, there is an escaping cone for light to be outcoupled into the air. The rays inside this cone can escape the LED, while the others are reflected back. The refractive indices of two media determine the cone's angle with respect to the surface normal (Θ_c). The mathematical description is based on Snell's Law (Eq. 3.5): [69]

$$\Theta_c = sin^{-1}(\frac{n_2}{n_1}) \qquad \text{Eq. 3.5}$$

Here, n_2 is the refractive index of air and n_1 is the refractive index of glass. The value of Θ_c for planar LEDs is usually between 20-30° meaning the light inside a cone of at most ~30° can escape the LED, and the rays with a higher degree would be reflected inside the structure. For isotropic EMLs –the case that the emission

pattern of EML is isotropic– the outcoupling efficiency has the value of 15-22% [36]. This means only 15-22% of generated photons inside the structure can outcouple to the air. Considering the Eq. 2.4 (i.e., EQE = IQE x $\eta_{out)}$, the maximum achievable EQE values are therefore limited by the outcoupling efficiencies. When using such light extraction features in the patterned surfaces, the total internal reflection decreases, leading to an increase in the amount of outcoupled light.

Chapter 3

EXPERIMENTAL METHODS

This chapter will discuss the experimental methods involving the CQWs synthesis process, self-assembly, fabrication of CQW-LEDs, and the various techniques for characterizing CQWs and LEDs.

3.1 Synthesis of cadmium myristate

The synthesis of core (CdSe) starts with the cadmium myristate (Cd(myr)), which is a white color substance. We synthesized Cd(myr) according to the previous recipes in the literature, with slight modifications [70]. In a typical synthesis, 2.46 g of cadmium nitrate tetrahydrate and 6.26 g of sodium myristate were dissolved in 80 and 500 mL of methanol, respectively. After 3 h stirring, they were mixed and kept stirring for 5 h. Then, a white color cadmium myristate was precipitated by centrifugation. The cadmium myristate powder was washed twice using methanol to purify and remove the impurities. Finally, the product was kept overnight under vacuum at room temperature and stored under ambient conditions.

3.2 Synthesis of 4 ML CdSe core CQWs

After Cd(myr) preparation, the four monolayers (ML) CdSe NPLs were synthesized according to a reported protocol. First, 24 mg of Se powder and 340 mg of cadmium myristate, and 30 mL of ODE were loaded into a 100 mL three-neck flask and degassed at 95 °C for 1 h. Then, under argon gas, the temperature was set to 240 °C. When the color of the solution changed to an orangish color around 195 °C, 120 mg of cadmium acetate dihydrate was added to the reaction. The solution was kept stirring at 240 °C for 8 min. Finally, the growth was terminated by adding 1.5 mL OA and quenched in a cold-water bath. The 4 ML CdSe NPLs purified through size-selective precipitation to obtain a monodisperse solution. The final product was redispersed in hexane and kept for further use.

3.3 Synthesis of CdSe/$Cd_{0.25}Zn_{0.75}S$ core/ hot-injection shell (HIS) CQWs

As mentioned in the literature review section, the core solely does not show sufficient PLQY for use in LED. Therefore, a shell coating of high band-gap material is mandatory. Here, we synthesized the high-PLQY core/HIS NPLs based on published protocols with slight modifications. The previously synthesized four-ML CQW solution in hexane, Zn-acetate (55 mg), Cd-acetate (22.5 mg), and ODE (7.5 mg) were added to a 25 mL flask and degassed for 1 h at ambient temperature and 30 min at 80 ℃. Then, under argon gas, 1 mL of OLA was added to the solution, and the temperature was set to 300 ℃. Starting from 165 ℃, the mixture of ODE (5 mL) and octanethiol (140 μL) was injected at a rate of 10 mL/h. Note that, after reaching 240 ℃, the injection rate was decreased

to 4 mL/h. After finishing the injection, the solution was kept for 1 h to complete the growth. The reaction was terminated by quenching with a cold-water bath. Then, the solution was washed by adding 5 mL hexane and 3 mL of ethanol. Finally, the NPLs redispersed in toluene and kept for the next step.

3.4 Ligand exchange of CQWs

We have followed a previously published protocol with slight modifications to change the as-synthesized OLA and OA ligands to the shorter ones. Under argon flows, 150 μL of 2-ethylhexane-1-thiol (EHT) ligands were added to 1 ML of NPLs in toluene solution (100 mg/mL) while stirring. Then the solution was kept stirring for 2 h under the gas environment to give the ligands enough time to be replaced by the as-synthesized ones. Then, NPLs were precipitated by adding ethanol and re-dispersed in toluene. The process was repeated twice to have a complete exchange, but in the second and third, 50 μL of EHT was added to the mentioned amount of CQWs. Finally, the resultant NPLs were washed by adding ethanol and re-dispersed in hexane.

3.5 Synthesis of $Zn_{0.95}Mg_{0.05}O$

In our LED architecture, we have used $Zn_{0.95}Mg_{0.05}O$ as an efficient electron injection layer. Here, to synthesize it, 2.95 mmol Zn-acetate dihydrates and 0.05 mmol magnesium acetate tetrahydrate were dissolved in 30 mL of dimethyl sulfoxide (DMSO) solvent and stirred vigorously (~1,000 rpm). Then, the mixture of 5.5 mmol tetramethylammonium hydroxide in 10 mL ethanol was injected into the Zn-acetate solution at a rate of 50 mL/h. Under the ambient conditions, the mixture was kept being stirred for 2 h. Afterward, the $Zn_{0.95}Mg_{0.05}O$

nanocparticles were precipitated by adding ethyl acetate and re-dispersed in ethanol. To improve $Zn_{0.95}Mg_{0.05}O$ nanoparticles' solubility, inside the nitrogen-filled glovebox, 200 μL of ethanolamine was added to the mixture and kept stirring for 2 h. Finally, the obtained $Zn_{0.95}Mg_{0.05}O$ nanoparticles were washed by adding ethyl acetate and re-dispersed in ethanol.

3.6 Device fabrication

After preparing the required materials, such as CQWs and ZnMgO, in the second step, we fabricated devices. The fabrication started with cleaning substrates, layer deposition, and finally encapsulation and measurement.

3.6.1 Substrate cleaning

We have used a pre-patterned indium tin oxide (ITO) coated substrates (see Figure 3.1) purchased from Ossilla with a sheet resistance of 20 Ω/square. They were cleaned in several steps: firstly, they were sonicated in distilled (DI) water and detergent (Hellmanex) solution for 15 min, then in DI water for 15 min, after that, in an acetone bath for 15 min and finally in an isopropanol bath for 15 min. At this point, the substrates were cleaned from any dust, oil, and packaging processes' contamination. The substrates were treated by ozone-plasma to clean any remaining organic substances thoroughly. We have used the Asher Ozon-plasma instrument for this purpose. Also, the highly active oxygen atoms in the oxygen plasma process could increase in magnitude the workfunction of the ITO layer. This enhancement in the workfunction of ITO decreases the barrier for holes to move from ITO to the HIL. However, the oxygen-plasma process can also increase the sheet resistance of the ITO, affecting the charge mobility. So, the

oxygen-plasma process should be carried out in an optimum duration and at optimal power levels. In our case, we have used 30 W for 10 min.

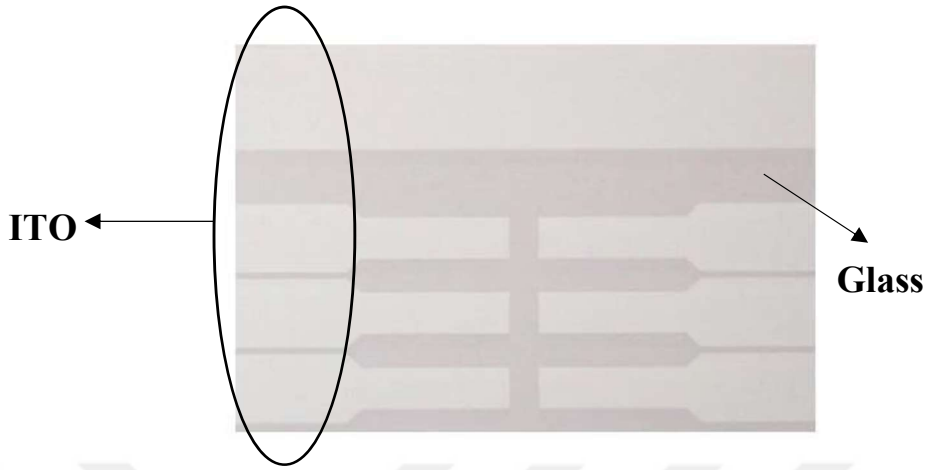

Figure 3.1: *Photograph of patterned ITO on a glass substrate.*

3.6.2 Layer deposition

As the first layer, the HIL of PEDOT:PSS has been deposited on the pre-patterned and cleaned ITO substrates using a spin-coater. Since the solvent of PEDOT:PSS was water, we could not carry out this process inside the glove box. The PEDOT:PSS was mixed with isopropanol in the ratio of 1:1. This mixing helps obtain a high-quality film since the isopropanol enhances the surface wettability. The mixture was filtered by 0.25 hydrophilic filters (PTFE membrane) to remove large aggregated polymer. In our work, we have used a spinner in the dynamic mode, in which the solvent is introduced to the substrate while rotating. The spinner's rate was set to 3,000 rpm for 45 s. After deposition, we had to bake them in the air at 120 ℃ for 30 min due to water in the PEDOT:PSS solution, which can cause moisture contamination in the glove box system.

After the first step in the air atmosphere, the PEDOT:PSS coated substrates were transferred to a nitrogen-filled glove box (O_2<0.1 and H_2O<0.1

ppm) and baked for 5 min at 110℃ inside the glove box to remove the possible absorbed moisture and oxygen while transferring. As the second layer, poly-TPD in the concentration of *8* mg/mL dissolved in chlorobenzene spin-coated at 2,000 rpm for 60 s. To prepare the poly-TPD solution, 8 mg of powder of the polymer was dissolved in 1 mLof chlorobenzene and kept being stirred for 24 h. After deposition of poly-TPD, the substrates were baked for 30 min at 110 ℃. Then, the PVK in the concentration of 2 mg/mL dissolved in 1-4 dioxane was spin-coated at 2,000 rpm for 60 s and then baked at 150 ℃ for 30 min. Noteworthy, solely for the PVK layer, we have used the spinner in the static mode in which the solvent is introduced to the substrate and then the spinner starts to rotate. Also, the solvent preparation for PVK was the same as poly-TPD.

After finishing the hole-side, the EML has been deposited. Then CQWs solution in the hexane with the concentration of 15 mg/mL was spin-coated on the PVK film. The NPLs were washed four times using antisolvent of ethanol to clean up all the remaining ligands. The rate of spinning was 2,000 rpm for 45 s. Then, to completely dry the substrates, they were baked for 30 min at 60 ℃. Following EML, the ETL of $Zn_{0.95}Mg_{0.05}O$ in the concentration of 25 mg/mL dissolved in ethanol was deposited by spin-casting at 2,000 rpm for 60 s and then was baked at 90 ℃ for 30 min. Finally, the substrates have been moved inside an oxygen-free thermal evaporation system (~9×10^{-7} torr) for deposition of the Al layer. Here, a shadow mask was used to make an active area of 4.5 mm^2. The substrates have stayed inside the chamber for 30 min to stabilize the vacuum level. After that, the deposition started, first with 10 nm of Al with a deposition rate of 0.4 °A/s and then the rate was increased to 10 °A/s to create a gleaming Al layer.

Finally, the devices were encapsulated by glass coverslip and UV-curable resin. After finishing the layer deposition, one droplet of UV-curable resin was added to the substrates' active area. Note that, to prevent the resin from covering the substrate's electrode area, the droplet should be as small as possible; it should solely cover the active area. Then a glass coverslip was put on the active area. Finally, the sealed devices stayed under the UV lamp for 30 min to harden the resin. Figures 3.2 a-b illustrates the steps of this process.

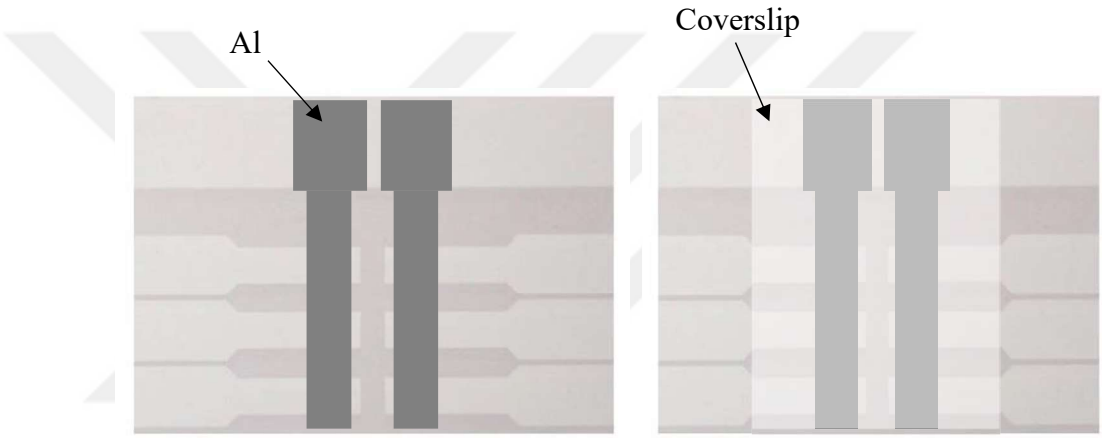

Figure 3.2: *Images of substrates a) before and b) after encapsulation.*

3.6.3 Oriented self-assembly

For fabricating the devices using the self-assembly process, after coating the hole injection layer (HIL) and hole transport layers (HTLs) inside the N_2-filled glovebox, we put the substrates into a Teflon container into which is poured the acetonitrile (ACN) subphase on an inclined stage (see Figure 3.3a). We used ACN as a subphase because it decreases the process's duration as it evaporates quickly; the process was completed in less than a minute. Subsequently, 20 μL of NPL in hexane solution with a

concentration of 25 mg/mL was dropped on the ACN subphase from the top of the container (see Figure 3.3b). The CQWs dispersed across the subphase surface as soon as they fell on the ACN. After evaporation of hexane, the CQWs created a uniform face-down membrane on top of the subphase. To transfer this film to the substrates, the ACN was drained through a needle from the bottom of the container and the film sank onto the substrate coated with the PVK layer on the top (see Figure 3.3c). Note that, for having a highly uniform film, the height of ACN on top of the substrate should be as low as possible to ensure the least amount of movement of the ensembled film while draining (see panel d in Figure 3.3a). Also, we have used silicone oil surfactant (see Figure 3.3b) to compress the SAM membrane further and avoid the crack and void formation during the deposition process due to capillary forces by the walls of the container. After draining the ACN, the substrates stayed in a vacuum chamber inside the glove box for 10 min for complete drying.

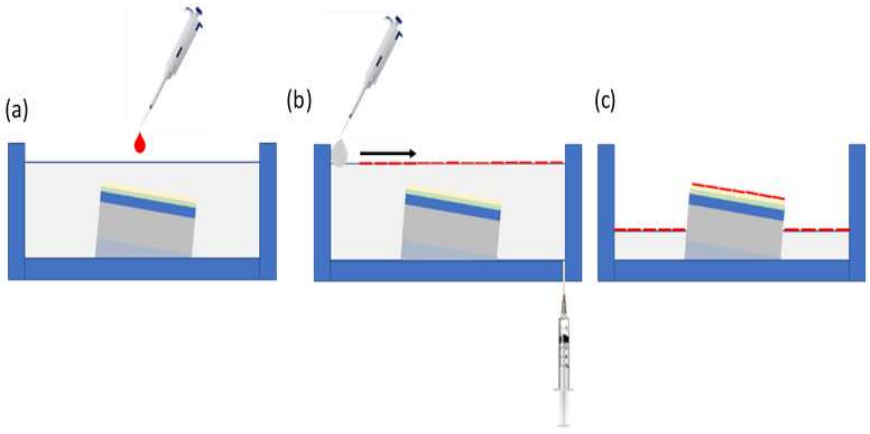

Figure 3.3: *Schematics of oriented selfassembly: a) the first step of the self-assembly process where the substrate is inserted into acetonitrile (ACN), being placed on an inclined stage, and*

NPL solution is dropped. b) Second step of self-assembly of dropping silicone oil surfactant for compresion and draining from the bottom using a syringe. c) Complete drainage of ACN and obtaining oriented NPL monolayer on the substrate.

3.7 Characterization

In this section, we describe various methods for analyzing the synthesized CQWs. Also, this section presents the details of the techniques we have used for analyzing the fabricated LEDs.

3.7.1 CQW's characterization

We have used several optical spectroscopic and imaging techniques to analyze the properties of CQWs.

3.7.1.1 Optical spectroscopy

The optical spectroscopy methods are non-destructive, noncontact, and fast techniques for analyzing the excitonic properties of the NPLs. These techniques usually use light-matter interactions for quantifying the behavior of CQWs. The most popular ones are photoluminescence (PL), absorption, photoluminescence quantum yield (PLQY), and Fourier-transform infrared spectroscopy (FTIR).

3.7.1.1.1 Photoluminescence (PL)

The instrument for PL measurement consists of two monochromators (emission and excitation), a light source, detector, and mirrors. In the PL excitation (PLE) measurement, the sample is excited at varied wavelengths and a detector collects the sample's emission. The wavelength that provides the highest emission

intensity is called the excitation wavelength. In the PL, by absorbing light of a specific wavelength (excitation wavelength), the electrons in the valance band of the sample are excited to the conduction band. Relaxation of these excitons results in the emission of light. This light is collected using a detector and presented in intensity as a function of the wavelength. We measured the PL spectra of NPLs using the Cary 100 photoluminescence spectroscopy instrument.

3.7.1.1.2 Absorption

Light can be scattered, absorbed, or transmitted when interacting with the material. The absorption spectra illustrate the portion of incident light which is absorbed. The instrument for this measurement usually works in the 200-1200 nm wavelength range. Depending on the material type, the absorption diagram shows some specific features, which is an indicator of material property. For example, in the CdSe NPLs spectrum, two excitonic (hh and lh) peak positions depend on monolayers' number. We have used the Cary 100 UV-visible instrument for absorption spectroscopy in our work. The sample measurement took place both in solution and on the film.

3.7.1.1.3 Photoluminescence quantum yield (PLQY)

The photoluminescence quantum yield (PLQY) technique measures the optical efficiency of colloidal nanocrystals (NCs). PLQY is defined as the ratio of the number of emitted photons from NCs in the unit of time per number of absorbed photons in the unit of time. This measurement could have been undertaken in two different methods: absolute and relative quantum yield. In the relative method, the PLQY of material is compared with a well-known material's PLQY. The

critical note on this method is that the concentration of two materials should be the same as well as the emission wavelength. In the absolute method, the PLQY of material is directly derived from emission and absorption spectra. In this method, a sample in a glass cuvette is placed inside an integrating sphere. In four stages, this measurement determines the PLQY of the NPLs: Firstly, the instrument measures the spectrum in the dark (no excitation light). Secondly, it measures the spectra when the sample is not placed in the integrated sphere with light. Thirdly, it measures the spectrum of the sample when it is excited directly. Finally, the detector measures the spectrum of the sample when it is excited by an indirect light (scattered one). The instrument then calculates the PLQY using the de Mello method [34]. In our work, for measuring the PLQY of the samples, we firstly diluted them to a concentration equal to the point of 0.08 absorbance. Then following these steps, we measured the synthesized sample's PLQY in solution and film.

3.7.1.1.4 Fourier-transform infrared spectroscopy (FTIR)

Fourier-transform infrared spectroscopy (FTIR) technique is a tool to acquire information about the nature of bonds in the organic (ligand) part of NCs. The term Fourier-transformation originates from the fact that the acquired data is the Fourier-transformation of the raw data. The working principle of this technique is similar to the UV-visible method. The instrument sends photons in the infrared region to the sample and measures the wavelengths of the absorbed photons. Finally, using the device library, the nature of bonds is derived. In our work, we have used this method to study the type of ligands of the CQWs. For measurement, we drop-casted the NPL's solution on top of the crystal of the

device and then waited for a few minutes to completly dry the sample and start the measurement.

3.7.1.2 Imaging techniques

Among the most commonly used imaging techniques for investigating the structure of NPLs are transmission electron microscopy (TEM) and scanning electron microscopy (SEM). Also, the emission directionality is detected by back-focal plane (BFP) imaging technique.

3.7.1.2.1 Transmission electron microscopy (TEM)

Transmission electron microscopy (TEM) is the most widely used technique for investigating the shape, size, and thickness of NPLs. Figure 3.4 schematically shows the various components of a TEM instrument. In this instrument, using high voltage (100-300 kV) and ultra-high vacuum, a column of electrons goes through an ultrathin layer of the material. The difference in the intensity of various target parts turns into a high-quality image. The resolution of detection in this method is 2-5 °A which is in the order of atomic distance. We have used this instrument to imagine the cross-sectional cut of our devices. Firstly, using a focused ion beam (FIB) instrument, we cut an extremely thin cross-sectional area of the fabricated LEDs. After sticking the sample to a copper grid, we took the TEM images of that area.

Figure 3.4: *Photograph of a transmission electron microscopy (TEM) instrument.*

3.7.1.2.2 Scanning electron microscopy (SEM)

Scanning electron microscopy (SEM) is another widely used method for the topographical investigation of NPLs film. This technique scans the surface of a film of a target material using a beam of electrons. Using the reflected electrons, SEM images the surface of a sample. The resolution of this instrument is in the range of 5-40 °A. Unlike the TEM measurement, the SEM does not require any specific sample preparation procedure. Usually, we have used the instrument in immersion mode, providing us with more detailed features in the resulting images.

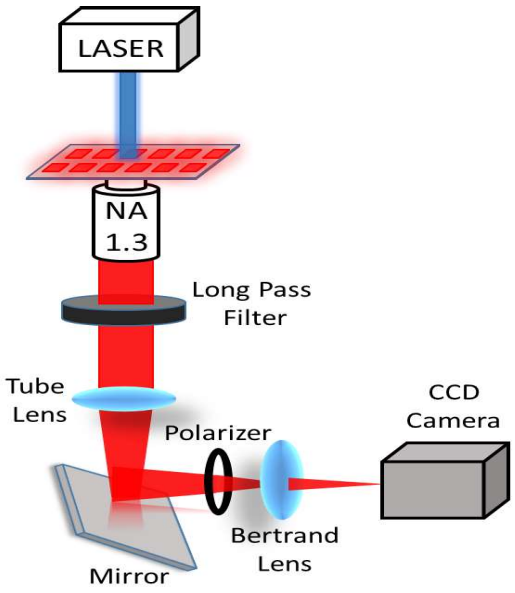

Figure 3.5: *Back-focal plane imaging setup.*

3.7.1.2.3 Back-focal plane imaging (BFP)

The back-focal plane imaging (BFP) technique provides information about the direction of emission from the film's surface of an emitter. It is the Fourier transformed image of the actual photograph. Figure 3.5 schematically shows the BFP setup used in our work. In this setup, we used a 400 nm laser beam for excitation and an inverted microscope system to take the BFP images. The components of the actual setup is presented in Figure 3.6.

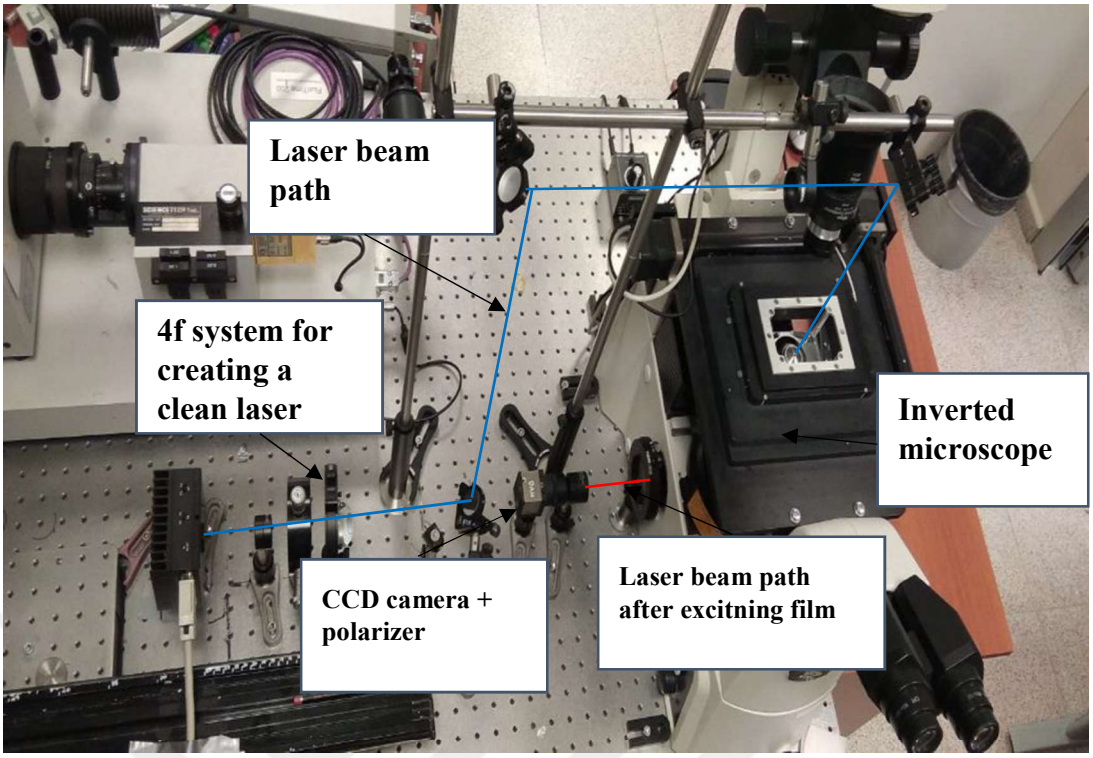

Figure 3.6: *Photograph of our used setup for back-focal plane (BFP) imaging with components indicated.*

Theoretically [37], [38], the relation between k and Θ is determined by the equation $k=n \sin(\theta)$, where n is the refractive index of immersion oil (n=1.52 in our experiments). In addition, the maximum k determines by the NA of the objective, which is k = 1.3. Experimentally, the transition dipole moments (TDMs) direction (Θ) is defined by the ratio of the horizontal ($p_{\parallel}$) component to the sum of the horizontal and vertical ($p_{\perp}$) elements ($\Theta = p_{\parallel}/ (p_{\parallel}+ p_{\perp})$). It has been reported that the in-plane (horizontal) orientation dipoles have a distinctive feature: the intensity is zero at $k_x/k_0=1$, where k_x and k_0 represent the photon momenta parallel to the substrate and in air, respectively. Using this feature, we determined the ratio of horizontal TDMs with respect to the total TDMs.

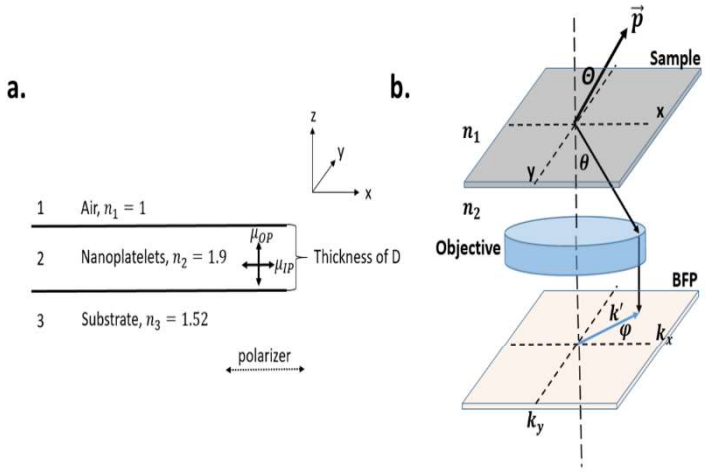

Figure 3.7: *Schematics of a) the three-layer structure of air, an NPL emitter layer and a substrate, and b) emission configuration indicating the coordinate system used for our calculations.*

3.7.1.2.3.1 Theoretical derivations

First, the emission pattern and dipole distribution were calculated theoretically using Schuller et al. [37] and Scott et al. [38], which provide detailed information about the derivation of the model. Using their final formulas, we found the ratio of the in-plane (IP) to out-of-plane (OP) TDMs direction. As illustrated in Figure 3.7, considering a structure including three layers, consisting of air, an emitting layer which is the NPLs, and a substrate as quartz, Fresnel reflection (r) and transmission (t) coefficients given in Eq. 3.1 and Eq. 3.2 describe the plane-wave reflected and transmitted between the interfaces ($i, j = 1,2,3$):

$$t_{ij}^{p} = \frac{2n_i n_j k_{zi}}{n_j^2 k_{zi} + n_i^2 k_{zi}}, \quad t_{ij}^{s} = \frac{2k_{zi}}{k_{zi} + k_{zj}}, \qquad \text{(Eq. 3.1)}$$

$$r_{ij}^{p} = \frac{n_j^2 k_{zi} - n_i^2 k_{zi}}{n_j^2 k_{zi} + n_i^2 k_{zi}}, \quad r_{ij}^{s} = \frac{k_{zi} - k_{zj}}{k_{zi} + k_{zj}}, \qquad \text{(Eq. 3.2)}$$

where n is the refractive index, k_z is the perpendicular components of momentum described by the equation $k_{zi} = \sqrt{k_0^2 \epsilon_i - k_x^2}$ where k_0 is the wavevector in air, and s and p indicate the polarization of the electromagnetic wave.

Then, the local densities of optical states for IP and OP dipoles were calculated using Eq. 3.3 and 3.5. Considering the effect of reflection on the interfaces and interference inside the emitter layer (Figures. 4.7 a-b), the density of photons in IP and OP are:

$$\rho_{IP}^{s} = p_x^s(k_x, k_y) = \left(\frac{1}{8\pi k_0^2}\right)\left(\frac{k_0}{k_{z3}}\right)\left|\frac{t_{32}^s e^{\frac{ik_{z2}D}{2}}\left(1 + r_{21}^s e^{\frac{2ik_{z2}D}{2}}\right)}{1 - r_{21}^s r_{23}^s e^{2ik_{z2}D}} \frac{k_y}{\sqrt{k_x^2 + k_y^2}}\right|^2 \quad \text{(Eq. 3.3)}$$

$$\rho_{IP}^{p} = p_x^p(k_x, k_y) = \left(\frac{1}{8\pi k_0^2}\right)\left(\frac{k_0}{k_{z3}}\right)\left|\frac{t_{32}^p e^{\frac{ik_{z2}D}{2}} \frac{k_{z2}}{n_2 k_0}\left(1 - r_{21}^p e^{\frac{2ik_{z2}D}{2}}\right)}{1 - r_{21}^p r_{23}^p e^{2ik_{z2}D}} \frac{k_x}{\sqrt{k_x^2 + k_y^2}}\right|^2 \quad \text{(Eq. 3.4)}$$

$$\rho_{OP}^{p} = p_z^s(k_x, k_y) = \left(\frac{1}{8\pi k_0^2}\right)\left(\frac{k_0}{k_{z3}}\right)\left|\frac{t_{32}^p e^{ik_{z2}D/2} \frac{k_x}{n_2 k_0}\left(1 + r_{21}^p e^{2ik_{z2}D/2}\right)}{1 - r_{21}^p r_{23}^p e^{2ik_{z2}D}}\right|^2 \quad \text{(Eq. 3.5)}$$

Based on the Eq. 3.4 and 3.5, the intensity of emission on the back focal plane with respect to IP or OP dipoles population and dipole moment (μ) are calculated by:

$$N^s(k_x, k_y) = A\rho_{IP}^s f_{IP}|\mu_{IP}|^2 \quad \text{(Eq. 3.6)}$$

$$N^p(k_x, k_y) = A\left(\rho_{IP}^p f_{IP}|\mu_{IP}|^2 + \rho_{OP}^p f_{OP}|\mu_{OP}|^2\right) \quad \text{(Eq. 3.7)}$$

where N is the calculated intensity of emission and A is the experimental fitting factor. Thus, the difference between 100% IP TDMs to the fitted curve has been measured by fitting the simulation curves to the experimental data.

3.7.1.2.3.2 **Light extraction efficiency calculations**

The LED structure's light-extraction efficiency (LEE) calculations were carried out using the finite-discrete time-domain (FDTD) method. Simulations were conducted by utilizing commercially available Lumerical FDTD Solutions (ANSYS Inc). To simulate the structure properly, thicknesses and refractive indices of each layer were determined from ellipsometry measurements.

The active region of the LED, which consists of NPLs, was modeled as electric dipoles. The dipole was placed in the center of the active layer. Metal boundary condition was used on the verge of the cathode layer. The other boundary conditions were selected as a perfectly matched layer (PML), which are perfect light absorbers. Since the area of the simulation region must be kept large enough so that fields radiated in the structure do not reach the absorbing boundaries, FDTD calculation was performed in a region with the dimensions of $10.00 \times 10.00 \times 2.29\ \mu m^3$.

The far-field projection was used to obtain the angular distribution of light in the substrate. Transmission coefficients at the interface between substrate and air were calculated using Fresnel's equations [5]:

$$t_{\perp} = \frac{2sin\theta_t cos\theta_i}{sin(\theta_i + \theta_t)} \quad \text{(Eq. 3.8)}$$

$$t_{\parallel} = \frac{2sin\theta_t cos\theta_i}{\sin(\theta_i + \theta_t)\cos(\theta_i - \theta_t)} \quad \text{(Eq. 3.9)}$$

where $t_{\perp}$ and $t_{\parallel}$ are the perpendicular and parallel components of the transmission coefficient, respectively. θ_i and θ_t are incident and transmission angles. From incident electric field and transmission coefficients, the angular distribution of the light in the air was found. Extracted power was determined by:

$$P_{ext} = \frac{1}{2}\sqrt{\frac{\epsilon_0}{\mu_0}}\iint |E_{air}(\theta,\phi)|^2 \sin(\theta)\, d\theta d\phi \qquad \text{(Eq. 3.10)}$$

Here $E_{air}(\theta,\phi)$ is the electric field in the air with a specific angle of direction.

Total extracted power from the orientation-controlled and that from randomly-oriented structures were calculated by repeating the above analysis for three fundamental dipole directions: 'x','y', and 'z'. From Figure 3.8, it can be seen that 'x' and 'y' orientations are parallel to the structure while 'z' orientation is perpendicular. To calculate light extraction efficiency, the results of each of these three analyses were multiplied with the ratio of dipoles in a specific orientation to all dipoles, added to each other (in the form of intensities), and divided by average dipole power [69].

To determine the ratio of parallel and perpendicular orientations of dipoles in a device, back focal plane spectroscopy was used [38]. The results show that while 92% of dipoles in the orientation-controlled structure are parallel to the device, in the randomly oriented structure rate of dipoles with parallel orientation is 67%.

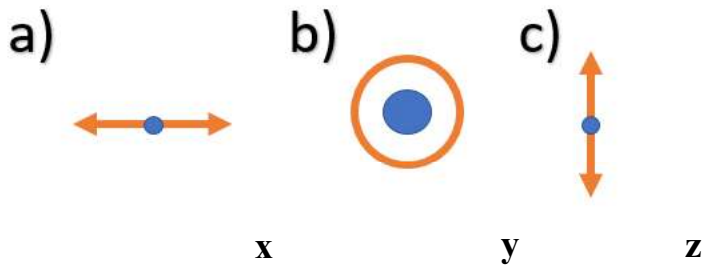

Figure 3.8: *Schematics of the dipoles modelled in a) x-direction, b) y-direction, and c) z-direction. x and y are parallel to the structure, while z is perpendicular.*

3.7.2 Device characterization

The performance measurements of the fabricated devices have been carried out using several methods and instruments. The external quantum efficiency (EQE), current density-voltage (J-V), electroluminescence (EL), luminescence (L), and angular emission intensity are the important properties that have been charcterized. Noteworthy, we took all the measurements in the air condition at ambient temperature after the devices were encapsulated.

3.7.2.1 External quantum efficiency (EQE)

As discussed in Section 2.3.4.5.1, the most important metric for measuring the efficiency of LED devices is the external quantum efficiency (EQE). Defined as as the ratio of the number of outcoupled photons per the number of injected electrons ($EQE = \frac{\#\ photons}{\#\ Electrons} \times 100$), in our setup we collected the outcoupled light using an integrated sphere. In the measurement, as shown schematically in Figure 3.9, we placed the LEDs outside the sphere so that the active area is in the middle of the window. Also, the hole size was relatively larger than the device's active area (from the light-emitting diode to the integration sphere), suggesting that the

coupling factor for the emitted photons in the forward direction was unity. The setup was a home-made system shown in Figure 3.9. Here, we coupled an integrated sphere (Newport 5.3") with Ocean Optics (QE-Pro) spectrometer. The system is connected to the software of the Ocean Optics spectrometer. The detector measured the outcoupled optical power. The total number of photons is calculated with the photon power based on the relation of $E = h\nu$. We recorded current density-voltage (J-V) data for the number of injected electrons.

3.7.2.2 *Current density-voltage (J-V)*

For J-V measurement, we used Agilent Technologies (U3606A) power source (see Figure 3.9). Similar to the spectrometer, the power source is connected to a computer system with custom software-design. The system measures the passed current at every applied voltage. Knowing the current and the number of electrons in the current unit (Ampere), the total number of electrons at each bias could be calculated. The software calculates the EQE at each applied voltage point by having the total photon number and the electron number.

3.7.2.3 Electroluminescence (EL)

Another essential characterization for LEDs is their emission wavelength and the spectral width of the emission profile. The same home-made setup for EQE in our work gives the EL diagram. The used spectrometer of the system calculates the EL spectrum across the wavelength range of 200-1200 nm.

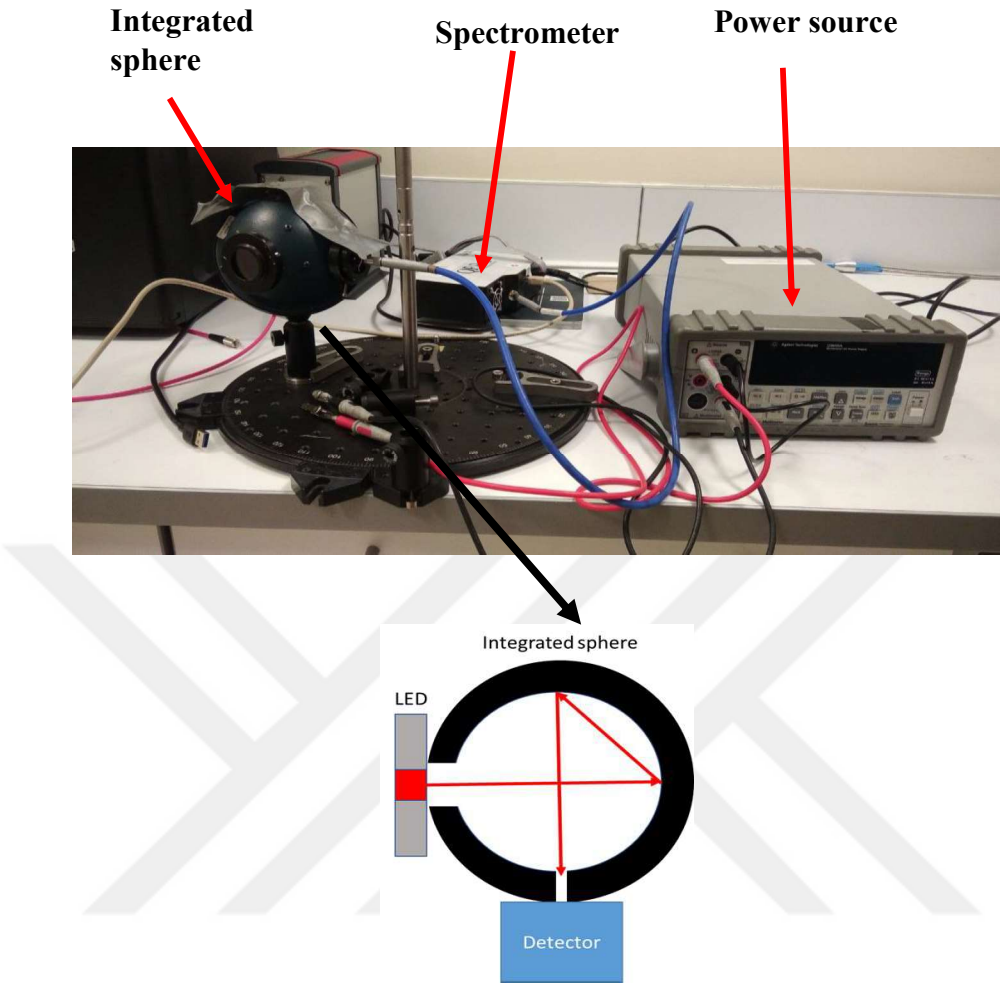

Figure 3.9: *Photograph of our home-made setup for measuring an LED's external quantum efficiency and current-density voltage (upper panel). Schematic illustration of the integrated sphere with the direction of rays traveling inside the sphere (bottom panel).*

Figure 3.10: *Photograph of our used radiospectrometer for brightness measurements.*

3.7.2.4 Luminescence

For luminescence measurements, we used a Konica Minolta CS-2000 spectroradiometer (see Figure 3.10). In this measurement, we fixed the LED to a flat surface vertically and connected it to the source. Then, we put the calibrated spectroradiometer at its focused distance, which is around 2 m away from the surface of the LED. The instrument was connected to a computer and operated with the software of the spectroradiometer (CS-S10W). This software provided the luminescence (L) in the units of cd/m^2, CIE coordinates of the collected light, the color of LEDs, and the temperature of that color.

The test-performing method is as follows: we first changed the voltage manually and took the current measurement at each voltage point. Then we repeated the process with 0.5 V increments. The reason for this type of manual recording was the time taken for luminescence measurement; measuring the brightness took about a few ms at each bias point.

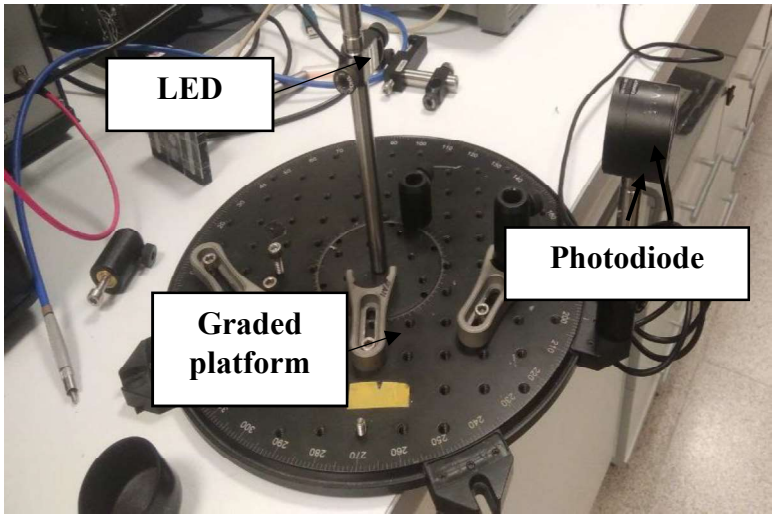

Figure 3.11: *Photograph of our spectroradiometer set-up used to measure an LED's brightness.*

3.7.2.5 Lifetime

The half-life time is the time it takes for LEDs to reach half of their initial brightness. As a standard metric, T_{50} is commonly taken at the initial luminance of 100 cd/m^2. Here, using the spectroradiometer, we measured the T_{50} of our devices. The test was the same as the one for brightness measurement. Here, we fixed the initial brightness of LEDs to the value of 5,000 cd/m^2. Then, for up to 10 min, we took measurements every 30 s. Then, we took the measurement every 5 min up to 100 min. We finally converted the experimental recording at 5,000 cd/m^2 to the T_{50} at 100 cd/m^2 using the relation of Eq. 3.11:

$$L_0{}^n T_{50} = L_1{}^n T \qquad \text{Eq. 3.11}$$

3.7.2.6 Goniometry measurement

The emission profile is a factor for determining the directionality of emission couplingout of the device, which is given as angular emission intensity profile. We calculated this emission pattern profile using goniometry measurements.

Here, as shown in Figure 3.11, we placed our LED in the middle around the graded platform where a calibrated Si photodiode (Newport) is mounted on the edge of this circle. Subsequently, we operated the LEDs at 5 V and recorded the total power from -90^0 to 90^0(across a total of 180^0 degrees). Note that 0^0 is where the surface of the detector and the LED are parallel. Immediately after turning on the LED, we took the measurement, then turned it off, and moved the detector by 5^0. This process has been repeated at every degree, from -90^0 to 90^0. Finally the recordings are constructed as the light power as a function of the emission degree in radial cordinates.

Chapter 4

RESULTS AND DISCUSSION

This chapter presents the results and discussion of the experiment and simulations including those of our synthesized CQWs and our fabricated devices. A large portion of which is taken from the arXiv article of ours \ Highly-directional, highly-efficient solution-processed light-emitting diodes of all-face-down oriented colloidal quantum wells by h. Dehghanpour Baruj et al., (https://doi.org/10.48550/arXiv.2201.08733) ([23]). (in submission)

4.8 Colloidal quantum wells (CQWs)

In this thesis, we synthesized square-shaped CdSe/$Cd_{0.25}Zn_{0.75}S$ core/hot-injection shell (HIS) CQWs (see Figure 4.1) previously developed by our group [16], [29], [54] with ligand modification. These CQWs consist of square-shaped cores coated with a gradient shell that has illustrated a high photoluminescence quantum yield (PLQY>95%) emitting at 650 nm with excellent chemical stability. The shell of $Cd_{0.25}Zn_{0.75}S$ was grown on the CdSe cores by adding the cadmium and zinc precursors at room

temperature and continuously injecting the sulfur precursor at higher temperatures (the hot-injection method). Details of the synthesis procedures of CQWs are given in the chapter 3. The outer shell structure ensures the confinement of the excitons inside the core region to impede nonradiative recombination by surface traps [23] [66]. The gradient structure of the shell also provides a low lattice mismatch between the core and the outer shell, which reduces interface defects and nonradiative recombination. Finally, the outmost layer consists of oleic acid (OA) and oleylamine (OLA) ligands [16], [49]. The role of these ligands is to allow for good solubility in the colloidal solution, which is a critical parameter for solution-processed fabrication techniques while passivating the surface defects. Thanks to their heterostructure, the obtained NPLs show a PLQY of 95% in the solution and 87% on the quartz substrate, which is the highest PLQY among all types of CQWs in the saturated deep-red color, with excellent chemical and optical stability [16], [24], [25], [54], [56]. However, the OA and OLA ligands of the as-synthesized NPLs have a very long organic tail. Resultantly, their length reduces the charge transport efficiency from the carrier transport layer (CTL) to the EML by enlarging the electron-hopping distance and creating a potential barrier for energy transfer. To address this issue, we switched the native long OA and OLA ligands with the shorter 2-ethylhexane-1-thiol (EHT) to reduce the energy barrier for the charge transport (for ligand exchange details, please refer to the SI). In a recent

study, Song et al. [49] reported a high EQE of 30.9% for red-QLED using the EHT ligands capped colloidal quantum dots.

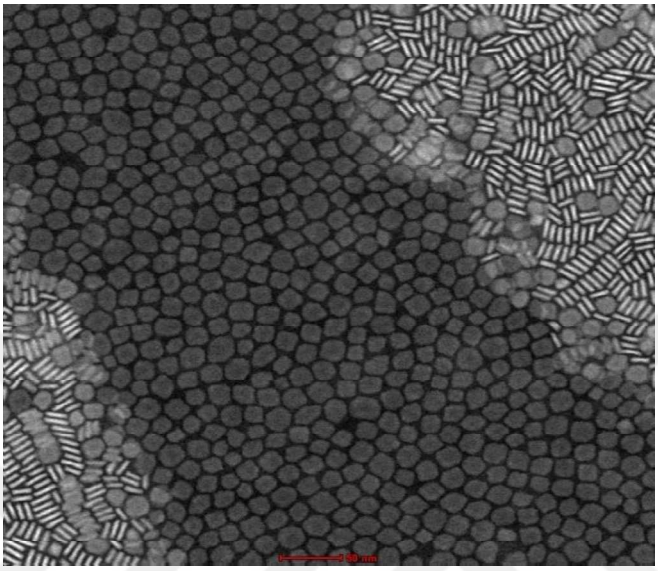

Figure 4.1: *Transmission electron microscopy image of our core/shell (HIS) CQWs.*

4.9 Ligand exchange

We changed the long native OA and OLA ligands to the shorter EHT ligands. Since the OA and OLA ligands of our as-synthesized NPLs have a very long organic tail, their length limits the charge transport rate from the carrier transport layer (CTL) to the EML, enlarging the electron-hopping distance and creating a potential barrier for energy transfer. Thus, we changed the native long OA and OLA ligands with the shorter 2-ethylhexane-1-thiol (EHT) to reduce this energy barrier for the charge transport. Song et al. [49] reported a high EQE of 30.9% for red-QLED using the EHT ligands on colloidal quantum dots.

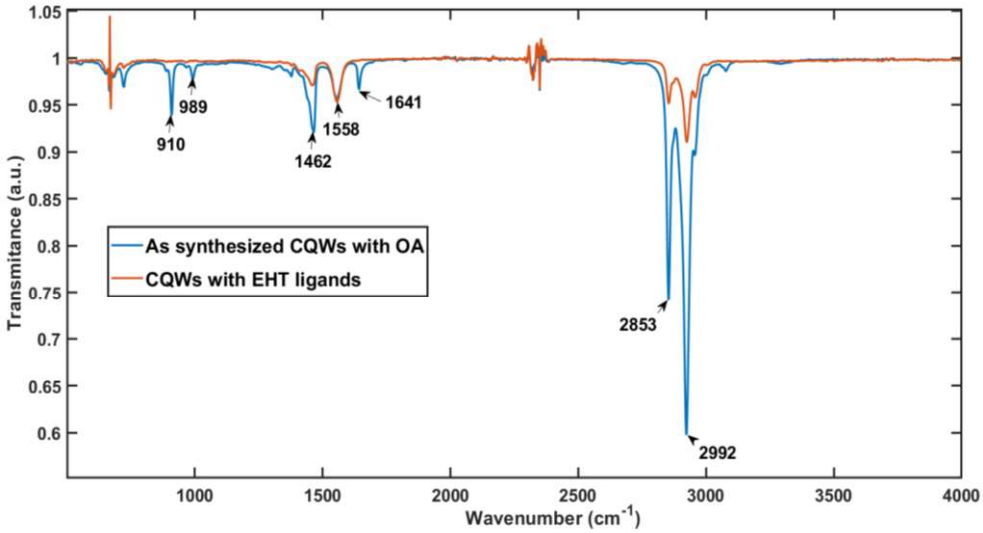

Figure 4.2: *Fourier-transform infrared (FTIR) spectra of our HIS-CQWs and LE-HIS-CQWs.*

To confirm the ligand-exchange process [15], [71], we took the Fourier-transform infrared spectroscopy (FTIR) (Figure 4.2) of the NPLs film from both the as-synthesized and the ligand-exchanged ones. In the FTIR spectrum, the bending vibrations of the amine group of OLA (located at 1,641cm^{-1}) of the HIS samples have disappeared after the ligand exchange (LE-HIS samples). We found out that the ligand-exchange process affects the electrical properties of NPLs without changing the optical properties. The photoluminescence (PL) and absorption spectra for the HIS and LE-HIS samples remained unchanged (see Figure 4.3a). However, the main effect of the switch of the ligands was on the valance band position of NPLs. We measured the band offsets using the XPS technique. Here, the XPS analysis of energy bands demonstrates the effects of ligands dipole. Figure 4.3b illustrates the proximity of the measured E_F-E_{VBM} for NPLs with OA (0.93 eV) and EHT (1.26 eV), suggesting that the ligand exchange barely perturbs the Fermi level of NPLs. However, the main difference has been detected in the secondary electron cut-off region, indicating the ligands' dipole

effect. Using two cut-off regions (Figure 4.3b) and Miller et al., [72] method and considering corrections [73], the calculated E_{VBM} values were ~5.93 and ~6.61 eV for the LE-HIS and HIS samples, respectively. Since the highest occupied molecular orbital (HOMO) of our used PVK was 5.8 eV, the potential barrier for the holes' movement from HTL to the NPLs is reduced from 0.87 eV in the HIS to 0.13 eV in the LE-HIS devices.

Moreover, the EHT ligands preserve the high PLQY of the emitters. In our case, the PLQY of ensemble NPLs remained as high as 88% after the ligand exchange. Even after six times washing, the PLQY decreased only to 85%. This observation confirms the robust attachment of ligands to the NPLs by the thiol group [49]. Also, the PLQY of NPLs with and without the ligand exchange in several substrates remained close (see Figure 4.3a).

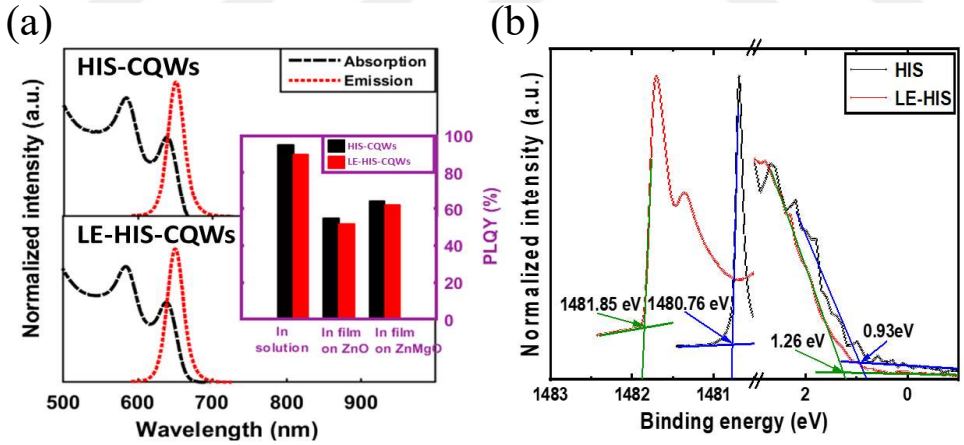

Figure 4.3: *a) Absorption and photoluminescence (PL) spectra of our hot-injection shell (HIS) grown (above) and ligand-exchanged (LE-HIS) (below) NPLs. Inset, PLQY of HIS and LE-HIS NPLs in solution, on ZnO film and* $Zn_{0.95}Mg_{0.05}O$ *film. b) XPS data the of second cut-off region (left-hand side) and the valance band region (right-hand side).*

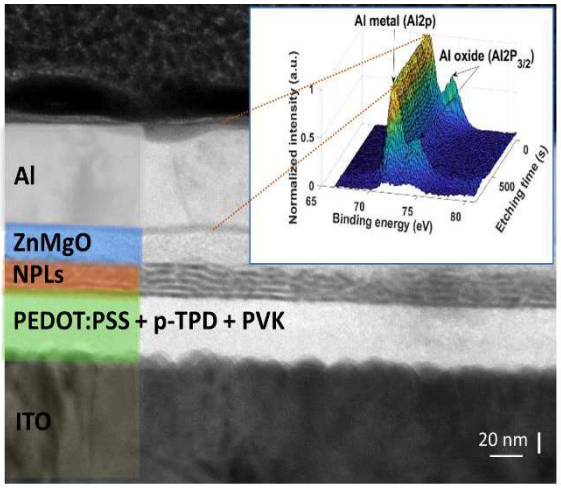

Figure 4.4: *Transmission electron microscopy (TEM) cross-sectional image of our device using the spin-coated hot-injection shell (HIS) NPLs; scale bar: 20 nm. Inset: 3D graph of X-ray photoelectron spectroscopy (XPS) depth profile of Al region with metallic and oxide Al peaks.*

4.10 Device structure

Our devices consist of indium tin oxide (ITO, 100nm)/poly(ethylene dioxythiophene):polystyrene sulphonate (PEDOT:PSS, 30nm)/poly (N,N9-bis(4-butyl phenyl)-N,N9-bis(phenyl)-benzidine) (p-TPD, 20nm)/ poly(9-vinyl carbazole) (PVK ,10nm)/NPLs (20nm) /$Zn_{0.95}Mg_{0.05}O$(30nm) /Al(100nm). (see Figure 4.4). All the layers were deposited using the spin-casting technique in dynamic mode except for the PVK layer, which was in the static mode. Herein, we took advantage of both the high hole mobility provided by poly-TPD (1×10^{-4} $cm^{-1}V^{-1}s^{-1}$) and the deep highest-occupied-molecular-orbit (HOMO) energy level (-5.8 eV) provided by PVK. This bilayer structure accompanied with PEDOT:PSS provides a stepwise energy level alignment between ITO and EML (see Figure 4.5).

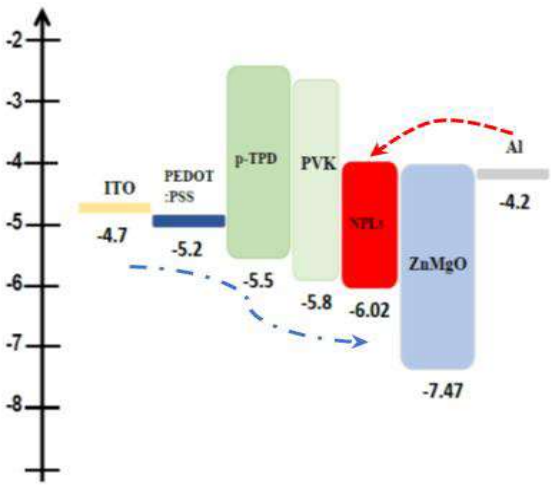

Figure 4.5: *Energy band diagram of the optimized structure.*

Moreover, as an electron transport layer (ETL), we used Mg-doped ZnO (5%) to diminish the exciton quenching [13], [33], [67], [74]. It is known that the direct contact of ZnO to NPLs quenches the emission due to the nonradiative energy transfer, but this phenomenon is significantly suppressed by doping Mg in the ZnO structure [67], [74]. To confirm this effect, we analyzed in-film PLQY of HIS NPLs on ZnO and $Zn_{0.95}Mg_{0.05}O$ layers. We found that in-solution PLQY of 95% for the NPLs dropped to 55% on ZnO and 64% on $Zn_{0.95}Mg_{0.05}O$. Therefore, this quenching limits the maximum achievable EQE based on the following relation [8], [16].

$$EQE = \eta_{out}.r.q.\gamma \qquad \text{(Eq. 4.1)}$$

Here, η_{out} represents the extraction efficiency, r represents the fraction of excitons with the probability of radiative recombination, q is the film PLQY, and γ represents the charge injection efficiency inside the device. Since the EQE and q are directly correlated, a decrease in q reduces the EQE.

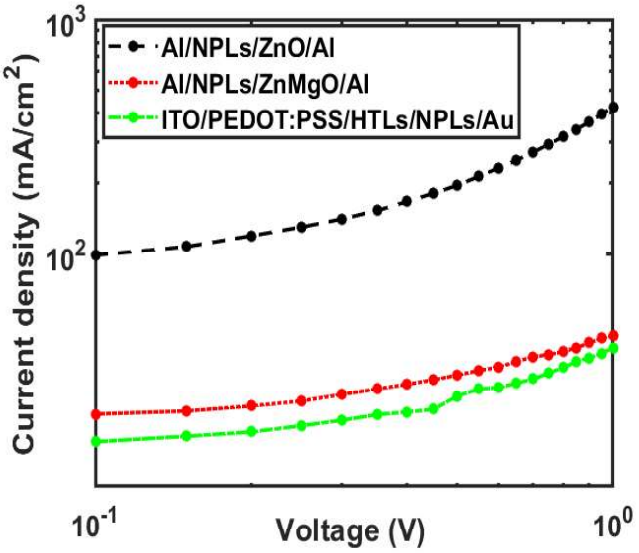

Figure 4.6: *Current density vs. voltages for the electron-only devices using the structure of Al/CQWs/ZnO/Al and Al/CQWs/ZnMgO/Al and the hole-only device using the structure of ITO/PEDOT:PSS/HTLs/CQWs/Au. Note that the thicknesses of all layers have been kept the same as those of our active device.*

The charge balance can be justified by checking the electronic and hole-only devices' current density versus voltage (J-V) curves (see Figure 4.6). The hole-only devices are the devices that consist of all the layers of electrode/HIL/HTL/EML/electrode. Our hole-only device is ITO/PEDOT:PSS/p-TPD/PVK/NPLs/Al. The hole-only device is a LED without EIL and ETL. This layer has been used for investigating the electrical performance of the layers. This layer could give information about the amount of passing charge, which helps to optimize the structure of the device. On the other hand, the electron-only devices are the ones with the structure of electrode/EIL/ETL/EML/electrode. In our case, the structure is Al/NPLs/ZnMgO/Al and Al/NPLs/ZnO/Al. The J-V curve of the electron-only device fabricated by $Zn_{0.95}Mg_{0.05}O$ is closer to the hole-only device's J-V than the electron-only device manufactured by ZnO nanoparticles.

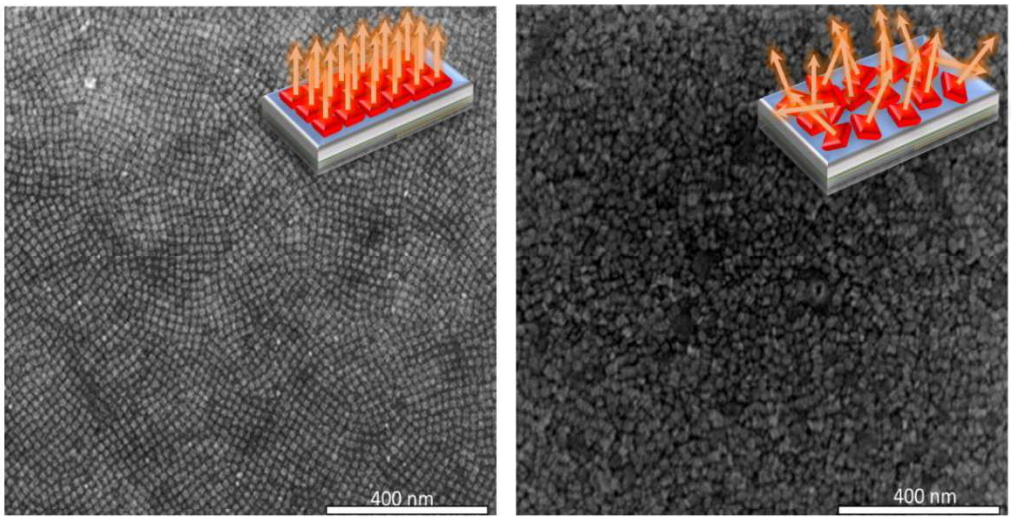

Figure 4.7: *Scanning electron microscopy (SEM) image of a) all-face-down self-assembled monolayer. Inset: the schematic of all-face-down SAM film of NPLs on the device's layers. b) SEM image of the spin-casted film of NPLs. Inset: the schematic of a spin-casted film of NPLs on the device's layer.*

4.11 XPS depth profile

Also, we have used the X-ray photoelectron spectroscopy (XPS) depth profiling technique to quantify the oxygen content in the Al layer and the Al and ZnMgO interface. In the analysis, we used an ion-beam for 10 seconds of etching duration and repeated it five times. The XPS depth profile results (see Figure 4.4) show some degree of oxidation in the Al and $Zn_{0.95}Mg_{0.05}O$ interface. This observation is related to the aging process. In this process, some oxygen atoms diffuse to the Al layer and make the Al_2O_3 compound. This compound has an insulator nature, which creates a barrier to transferring charges. So, it could increase the efficiency of devices by acting as an electron blocking layer for balancing the charges [15], [68]. However, in our case, we have not observed such an effect. Here we conclude that utilizing the $Zn_{0.95}Mg_{0.05}O$ nanocrystals as an ETL is preferable to the ZnO nanocrystals in our devices.

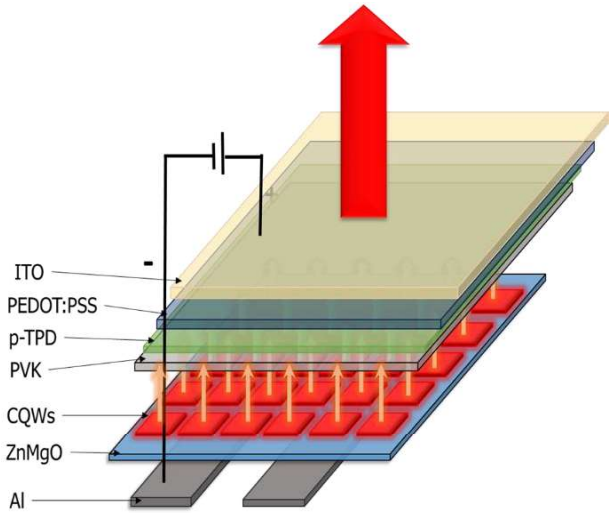

Figure 4.8: *Schematic of our oriented-CQW-LED structure.*

4.12 CQWs self-assembly

Figure 4.7a shows the scanning electron microscopy (SEM) image of the mosaic-like structure of the SAM film, which is highly uniform with a full surface coverage of NPLs on top of HTL compared to the spin-casted film of NPLs that are randomly oriented (see Figure 4.7b). The image also indicates a successful deposition of an all-face-down film on top of LED's layers which has not been reported yet. Thus far, film deposition has been carried out on silicon or quartz substrates. As shown in this image, there are almost no empty places in the deposited film, which is highly advantageous for optoelectronic applications. The pinholes typically lead to a charge leakage where the electrons pass the device structure without being recombined with the holes. It has been reported that the charges tend to pass the lowest energy potential area, which a pinhole provides such an area in the LEDs [60]. As a result of the self-assembly, we expect to observe a

limited amount of empty places in the EML and a high degree of recombination probability.

Moreover, Figure 4.7 illustrates schematically the expected direction of emission coming out of the oriented film and randomly oriented ones. From the SAM film, the light emitted in the direction normal to the surface of NPL, which is called as out-of-plane emission. As a collective behavior, the complete film exhibits the directional emission due to a perfectly aligned CQWs provided by self-assembly as it has shown.

Figure 4.8 schematically demonstrates the fabricated LED's final structure with the expected light emitted from the SAM film. Here, we illustrated the expected emission from the SAM film inside the LED's architecture. As it is conclusive here, the light will be directed inside the structure with slight diffraction due to the different properties of different layers.

In addition, to quantify the effects of SAM film on the properties of LEDs, we fabricated devices using a spin-coating technique as a standard sample with the same variables and structures as the LEDs with SAM film, where fabrication was carried out simultaneously. Also, as shown in Figure 4.7, we expect to observe a more anisotropic emission from this film where the light propagates through the layer with a standard Lambertian pattern. This structure has an outcoupling efficiency of 15-22%. It means that more than 22% of the created light inside the LED structure can escape. So, in an

ideal case where the IQE is 100%, the maximum achievable EQE would be 22%.

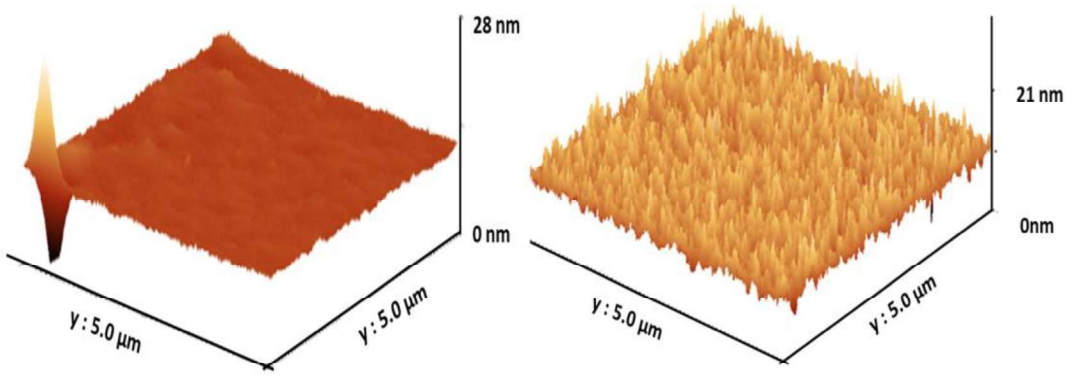

Figure 4.9: *Atomic force microscopy (AFM) images of a)our SAM NPL film and b) our spin-coated NPL film on the hole transport layer (HTL).*

Figure 4.9 shows the atomic force microscopy (AFM) measurements from the SAM film and the randomly-oriented film of CQWs. As shown here, the RMS roughness of the SAM film is <1 nm whereas this is >2.4 nm in the case of the spin-coated one. One of the biggest disadvantages of the CQWs compared to the spherical nanocrystals (QDs) is otherwise high RMS of their deposited film, which is related to their quasi-2D shape. Here, the resulted RMS for our SAM film is comparable with that of the spherical nanocrystals. Therefore, the charge injection efficiency in the case of using this in the EML of the LED is expected to be high. It is noteworthy to point out that, these results imply that the orientation-controlled film yields the lowest possible surface roughness, which is on par with that of spherical nanocrystal film.

Figure 4.10 demonstrates the potential effects of ACN solvent on the electronic properties of HTLs and HIL. Here, we fabricated hole-only devices with the structure of ITO/PEDOT:PSS/p-TPD/PVK/NPLs/Al. The layers were

deposited by the spin-coating process except for Al, which was deposited by thermal evaporation. In this device, after depositing the ITO/PEDOT:PSS/p-TPD/PVK layers, we placed the sample inside the ACN for 5 min and then baked it for 30 min at 90 °C. Finally, the NPLs were coated on the samples, followed by Al deposition. As shown in Figure 4.10, no apparent changes were detected in the hole-only device's current density versus voltages (J-V) characteristics with and without drowning in ACN.

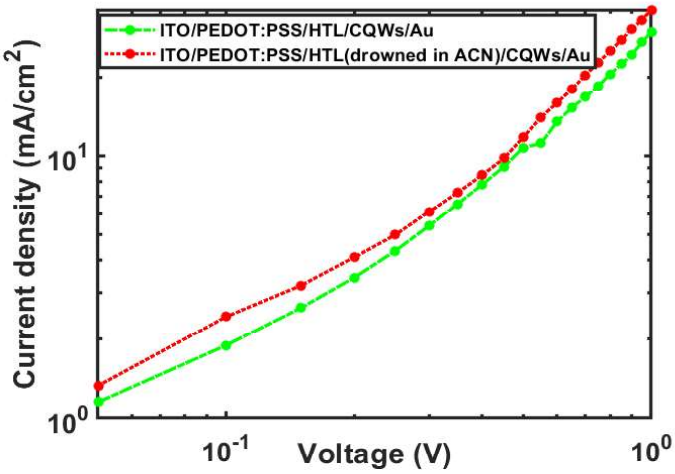

Figure 4.10: *Current density vs. voltages for our hole-only device in the structure of ITO/PEDOT:PSS/HTLs/CQWs/Au with and without drowning into acetonitrile (ACN).*

4.13 Back-focal plane imaging

From the all-face-down SAM film, as shown schematically in Figure 4.8, we expect to obtain a more directional emission profile than that of the randomly-oriented one. Since CQWs possess nearly all in-plane (IP) transition dipole moments (TDMs), their all-face-down ensemble film should act as an anisotropic emissive film. To realize the direction of emission (Θ) of the deposited all-face-down, single monolayer, CQW film, we have used the back-focal plane imaging

technique. In this imaging, we found the ratio of the horizontal ($p_{\parallel}$) component to the sum of the horizontal and vertical ($p_{\perp}$) elements ($\Theta = p_{\parallel}/ (p_{\parallel}+ p_{\perp})$) which experimentally gives the direction of TDMs. Figure 3.5 illustrates the schematic of our BFP setup. In this experiment, spin-casted and single monolayer self-assembled films of NPLs on 200 μm thick quartz substrates were excited by a 400 nm laser and a CCD camera took the back-focal plane images.

Figures 4.11a-b show the simulated intensity profile for fully in-plane (IP) and out-of-plane (OP) TDMs with the k_x-intensity diagrams for the p-polarized emission, given next to the images, respectively. The BFP images of self-assembled single monolayer and spin-coated samples with the k_x-intensity diagrams for the p-polarized emission are provided in Figures 4.12 a-b. We used the intensity diagrams of fully IP and OP and fitted them to the self-assembled film's intensity diagram (see Figure 4.12a). Here, we put all of the three normalized diagrams on top of each other so that the midpoints ($k_x/k_0 = 0$) of all three touch. Then, the $k_x/k_0 = 1$ for fully IP becames zero. For fully OP, this is 100 %. The distance between these two is some non-zero and non0unity IP TDMs percentage.

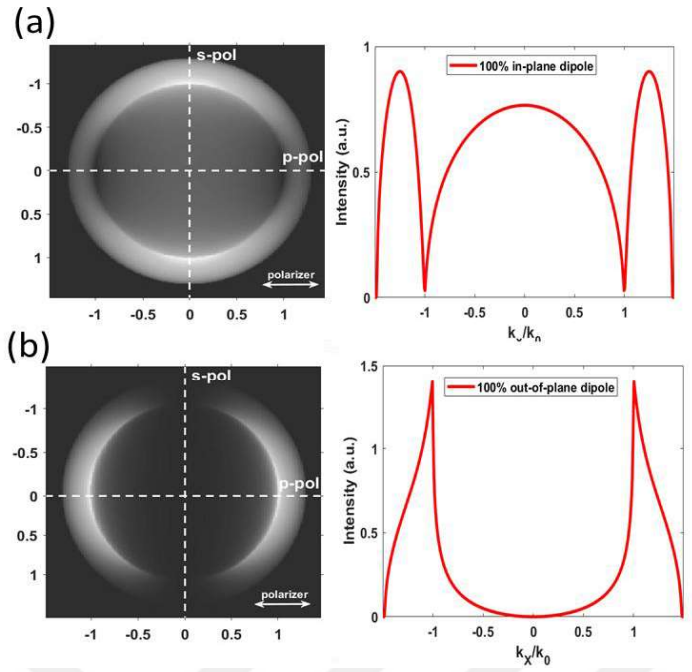

Figure 4.11: *Emission profile and intensity diagrams of a) fully IP TDMs, and b) fully OP TDMs.*

With that definition, we found Θ equal to 92%. By repeating the same process for the randomly-oriented samples (see Figure 4.12b), we found Θ is equal to 67% (see section 3.7.1.2.3 for the measurement and simulation details). Scott et al. [38] reported that Θ was 95% for all-face-down CdSe NPLs and Shendre et al. [24] found Θ of 91% for all-face-down CdSe/CdS@ CdZnS. Our measured Θ agrees with these results in the literature. These results confirm that in the all-face-down SAM film, a bright plane is directed toward the glass.

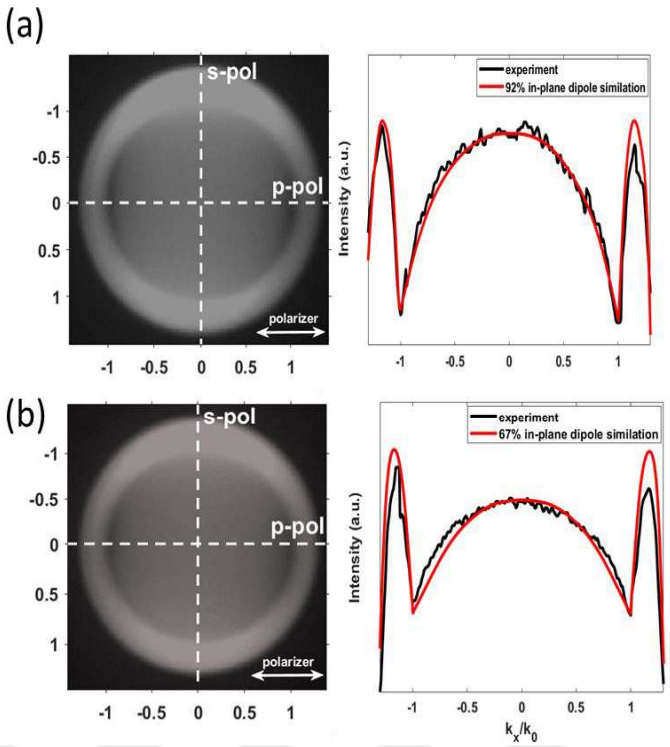

Figure 4.12: *Emission profile and intensity diagrams of a) our self-assembled NPL monolayer film on a quartz substrate with 92% IP TDMs fitting curve and b) our spin-casted NPL film on a quartz substrate with 67% IP TDMs curve.*

Based on the measured Θ values, we calculated the light outcoupling efficiencies using the finite-discrete time-domain (FDTD) method of commercially available Lumerical FDTD solutions (ANSYS Inc) (for simulation details, refer to section 3.8.1.2). We entered the thickness and material properties of the hole side (as it is the side on which lights are outcoupled) into the Lumerical and calculated the outcoupled light percentages. The calculated outcoupling efficiency for the device fabricated by an orientation-controlled NPL film with Θ = 92% was 34%. In contrast, it was 22% for the control sample made by spin-casting, with Θ being equal to 67%. Here, we calculated a significant enhancement of 54.5% in the outcoupling efficiency.

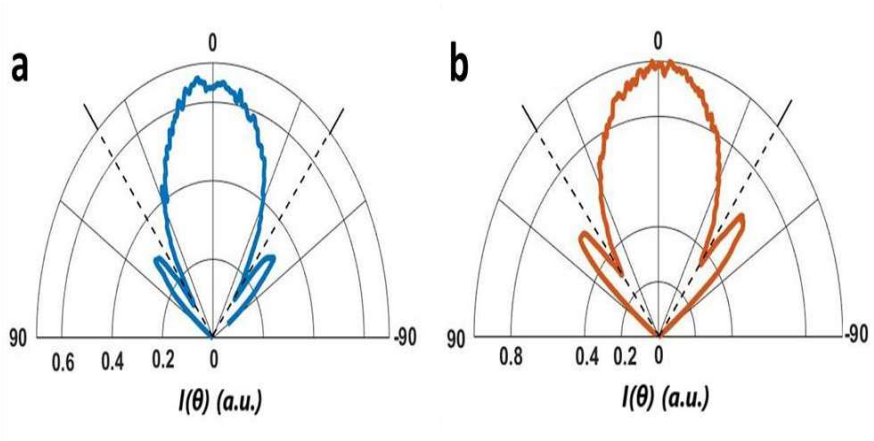

Figure 4.13: *Angle-dependent intensity profile for a) our self-assembled monolayer (SAM) of NPLs and b) the spin-casted NPLs film.*

In addition, Figures 4-13a-b show the angle-dependent profile for both our SAM and spin-coated films. The emission patterns give information about how relatively narrow the emission could be when using the SAM film opposed to the spin-coated one. As a result of this analysis, the diagram of Figure 4-13a clearly indicates that the emission coming from the SAM is narrower than that from the spin-coated one depicted in Figure 4-13b. This result is another proof of the directionality of emission of the SAM film. Also, the depth of the diagram of the SAM film in Brewster's angle (42^0) equivalent of the $k_x/k_0 = \pm 1$ is more than that in the spin-coated films. This finding demonstrates the high degree of IP TDMs coming from the SAM film.

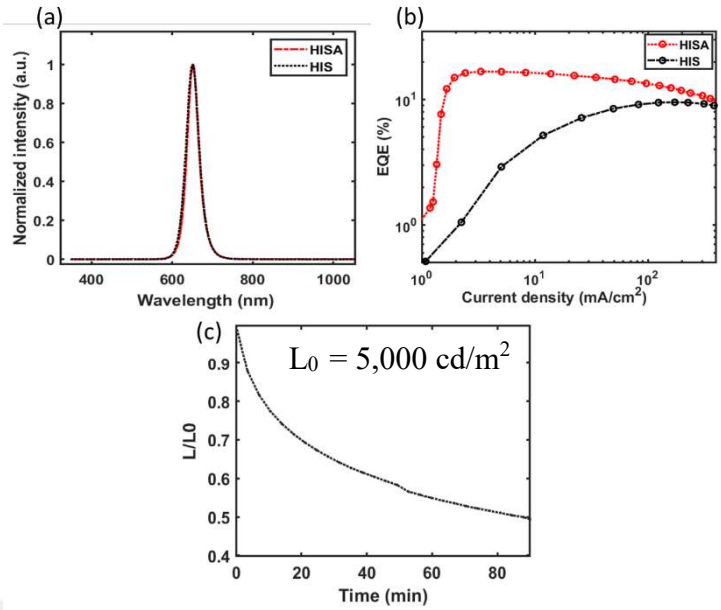

Figure 4.14: *a) Normalized electroluminescence (EL) intensity spectra for our HISA and HIS devices. b) EQE versus current density for the HISA and HIS devices. c) Stability data from the HISA device, starting at luminance of 5,000 cd/m².*

4.14 Performance of devices fabricated using HIS CQWs

To study the performance of devices, we have fabricated CQW-LEDs using SAM film of our HIS NPLs and the spin-coated ones as a control set. The normalized EL spectra (see Figure 4.14a) for the device fabricated using the all-face-down orientied self-assembly (HISA) and randomly-oriented spin-casting (HIS) film of NPLs exhibit the same emission peaks at 651 nm without any shift in the spectral position. Also, efficiency graphs (see Figure 4.14b) illustrate a peak EQE of 16.3% and 9.5% for the HISA and HIS, respectively. By comparing two devices, we detected a 71.5% enhancement in EQE. Based on our calculations, 54.5% of this improvement resulted from the enhanced light-outcoupling and the rest of 17% is attributed to the facilitated charge injection and reduced reabsorption in the case of using an ordered single monolayer of CQWs. As shown in Figure 4.14b, the HISA device has reached its maximum EQE at lower current densities

than the HIS ones. This observation indicates the facilitated charge injection is favored by the self-assembly.

Our devices are simply sealed with a glass coverslip and ultraviolet-curable resin, delivering good ambient stability. The half-lifetime (T_{50}), defined as the time duration for emitters to reach half of the initial brightness ($L_0/2$), for the HISA devices that measured at the initial luminance of 5,000 cd/m^2, was T_{50} = 89 min (see Figure 4.14c). Using the formula of $L_0^n T_{50} = L_1^n T$ [7], [16], [49], [63], [65] and assuming an acceleration factor of n = 1.5, we estimated the lifetime of 525 h at an initial luminance of 100 cd/m^2. Kelestemur et al. [32] reported a peak EQE of 9.92% for all-solution-processed CQW-LED using CdSe/CdS@CdZnS core/crown@HIS with a T_{50} of 560 h. Giovanella et al. [6] reported a device with a maximum EQE of 8.39% using CdSe/CdZnS core/HIS and a peak brightness of 1,500 cd/m^2. Thus far, our HISA devices show the highest EQE among the all-solution processed CQWs. However, the maximum EQE value is still lower than the record reported for CQW-LEDs [16].

4.15 Performance of devices fabricated using ligand exchanged CQWs

4.15.1 Electroluminescence and CIE

The normalized EL spectrum (see Figure 4.15a) of devices fabricated using the SAM film of our LE-HIS NPLs (LESA) peaks at 651 nm, corresponding to a CIE coordinate of (0.710,0.289) (see Figure 4.15b), which is relatively close to the color point of (0.708, 0.292) refered to as saturated red color. This CIE is ideal for new-generation ultra-high-definition television (UHDTV) applications [16],

[49], [65]. The inset photograph is taken from our LESA device operating at 5.0 V. Moreover, Figure 4.15c present the changes of the CIE coordinates (in both x and y) with changing the luminescence of the devices fabricated by SAM film of CQWs. Here, these diagrams demonstrate the outstanding color stability of the devices. This metric is highly desirable for applications.

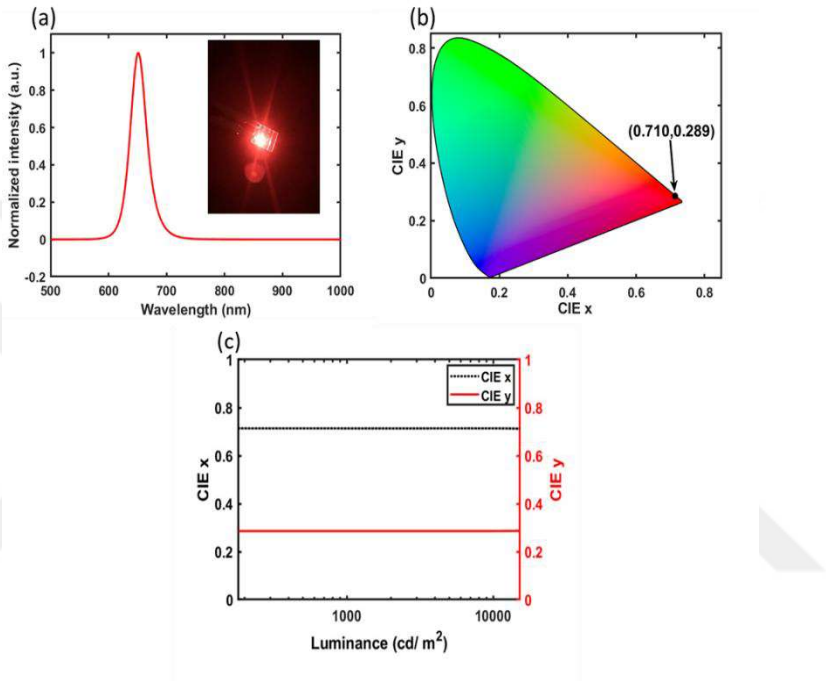

Figure 4.15: *a) EL spectra of the LED fabricated using self-assembly and ligand exchange (LESA). Inset: photograph of the device operating at 5.0 V. b) Corresponding CIE coordinates on the color gamut and e) CIE coordinates as a function of the operating luminance.*

4.15.2 Current density and luminescence

Figure 4.16a demonstrates the current density (J) flowing the SAM-CQW-LED structures under various voltages. As shown here, this graph firstly exhibits an abrupt increase in the current once it reaches the sub-bandgap turn-on voltage of ~1.7 V, showing a typical diode behavior. This behavior is a common shape of the J-V diagram of diodes. As a result, our devices possess a normal diode-like

behavior. Also, the SAM-CQW-LEDs provide a maximum brightness of 19,800 cd/m^2 at 8.0 V. In CQW-LEDs having high brightness and high efficiency simultaneously is difficult. However, from our SAM-CQW-LEDs, we observed outstanding brightness, which is comparable with the ones of OLEDs, QLEDs, and Pero-LEDs.

4.15.3 EQE

A peak EQE value of 18.1% at a current density of ~2.36 mA/cm^2 has been measured for our devices (see Figure 4.16b). This value is the highest reported EQE for all-solution processed CQW-LEDs thus far to the best of our knowledge. The J_{90} the current density in which EQE drops by 10% is 95.58 mA/cm^2 this correspond to an outstanding level of stability with low-efficiency roll-off. Also, the histogram of 35 devices shows an average peak EQE value of 16.8%, suggesting reasonable device reproducibility. Using the LE-HIS film of our NPLs, we observed statistically an 11% improvement in the EQE compared to that the HIS NPLs on the average.

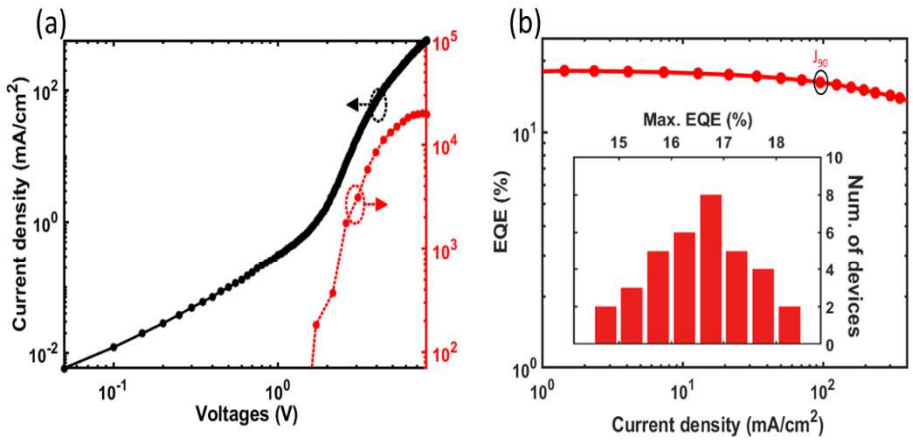

Figure 4.16: *a) Current density vs. voltage and luminance vs. voltages of our LESA devices. b) EQE vs. current density of the LESA devices with J_{90}. Inset: histogram maximum EQE of measured from 35 LESA devices.*

4.15.4 Goniometry measurement

Figure 4.17 shows the emission pattern of our LES and LESA devices performed by goniometry measurement alongwith a theoretically perfect Lambertian emission profile. As shown in this figure, the emission pattern of the devices fabricated by SAM film (SAM-CQW-LEDs) is narrower than the LES, and both are narrower than the ideal Lambertian emission. This finding indicates that in the oriented CQW-LEDs, the directionality of emission provided by the SAM film has been preserved in the device.

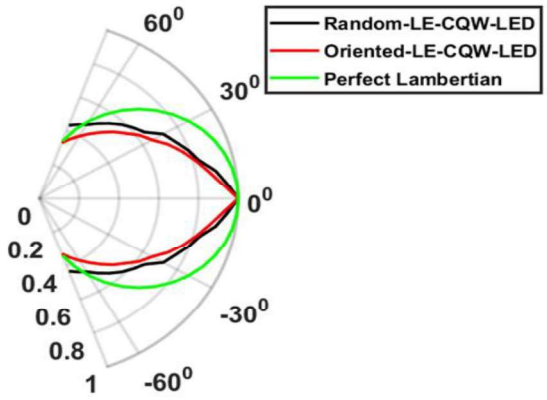

Figure 4.17: *Emission patterns of the LESA, and LES devices, alongwith that for simulated perfect Lambertian emission.*

4.15.5 Stability

Then devices were also simply sealed with a glass coverslip and using ultraviolet-curable resin, resulting in good ambient stability. The half-lifetime, measured at the initial luminance of 5,000 cd/m^2, is T_{50} = 42 min (see Figure 4.18a). Using the relation of $L_0^n T_{50} = L_1^n T$ [7], [16], [49], [63], [65] and again assuming an acceleration factor of n = 1.5, we estimate the lifetime of 247 h at an initial luminance of 100 cd/m^2. Our reported lifetime is 19-fold longer than the record organic-inorganic CQW-LEDs [16], but it is shorter than the HISA devices. The accumulation of charges in the EML due to shorter ligands and heating issues are attributed to be the main reasons for this relatively shorter T_{50} compared to the HISA devices.

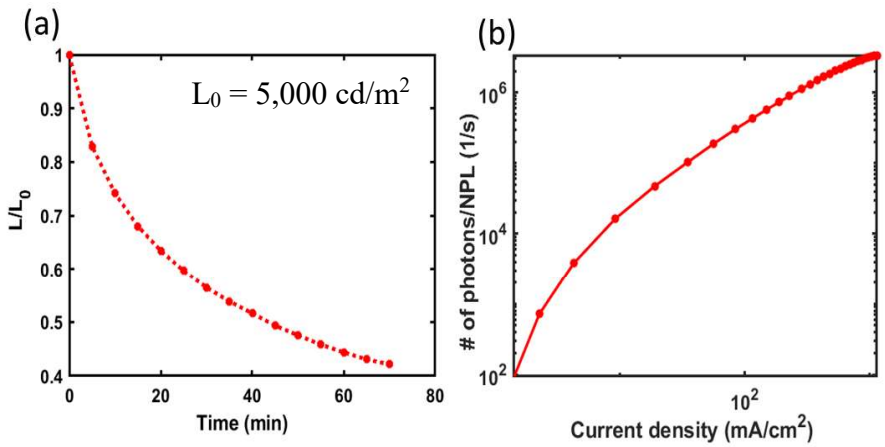

Figure 4.18 a) *Stability data from the LESA device starting at the luminance of 5,000 cd/m^2. b) Number of outcoupled photons per NPL vs. current density obtained from the LESA* device.

4.15.6 Photon per NPLs calculation

Moreover, the self-assembled monolayer film of NPLs enables us to explore the number of generated photons per individual NPL under current injection. Since the liquid-air self-assembly yields a uniform ensemble film, we were able to calculate the number of NPLs inside the active region of the devices. Using SEM images (see Figure 4.7) and image analysis software (ImageJ), we have found ~13×10^9 NPLs inside the device's active area (4.5 mm^2). Figure 4.18b shows the number of outcoupled photons per NPL versus current density. At the maximum EQE, we have ~2,180 photon/NPL per unit time. Considering the exciton lifetime of ~10 ns in NPLs [16], [54], we have calculated ~2×10^{-5} photon/NPL at a given time. However, this is the number of outcoupled photons, and to calculate the exciton number, we have calculated the internal quantum efficiency (IQE) using the equation of EQE = IQE×η_{out} [16]. Since the η_{out} is 34%, we have found ~6×10^{-5} exciton/NPL at a given time. This result shows that we are in the single excitonic regime in our LEDs. Also, this value at the maximum current density is ~9×10^{-2}

exciton/NPL, which still is in the single exciton regime. It has been reported that for an amplified spontaneous emission (ASE), 2-5 exciton/NPL is required [3], which is two orders of magnitude higher than the current density achieved in this study.

Chapter 5

CONCLUSIONS

In this work, for the first time, we showed successful fabrication of CQW-LED using the oriented self-assembly method. Here, we deposited the EML of a solution-processed LED using the liquid-air self-assembly technique. This provided a highly uniform, pinhole-free, all-face-down film of CQWs. Using this method, we aimed to exploit the direction-dependent properties of the CQWs in an active device, which was not possible with the conventional deposition method of spin-coating as this type of coating generates randomly-oriented NPL film. For EML, the used NPLs were in the form of core/hot injection grown shell with a high PLQY (>90%). This class of CQWs has shown the highest performance in the saturated red color thus far.

To further modify the electronic properties of our CQWs, we have changed their original OA and OLA ligands to shorter EHT ones. This process was performed specifically to shorten the ligands of CQWs and thus modify the E_{VBM} without changing their optical properties. For creating a uniform face-down film of

CQWs, we selected the liquid-air interface self-assembly with acetonitrile subphase. This method did not show any noticeable effect on the LED's other layers (HTL, HIL, and ETL). Also, the process duration was short, only about 1 min.

As a result, we achieved highly efficient all-solution-processed CQW-LEDs with a record high EQE among solution-processed devices, in the saturated red with excellent stability and a long lifetime. Such an impressive level of electroluminescence performance results from the highly directional emission originating from a high degree of in-plane transition dipole moments of the orientation-controlled single monolayer film of NPLs in the EML of devices. This film enables a 65% enhancement in the EQE compared to the randomly-oriented (spin-casted) one. Also, this NPL film yields the lowest possible surface roughness among all other deposition methods and enhances the charge injection efficiencies. In addition, changing the native OA and OLA ligands with EHT leads to a densely-packed film of these NPLs and improves the charge injection rate by shortening the hopping distance. By implementing the orientation-controlled film of such ligand-exchanged NPLs in the devices, we demonstrated a high EQE value of 18.1%, with a peak brightness of 19,800 cd/m^2 in an extremely saturated red color at a CIE coordinate of (0.710, 0.289) with a T_{50} of 247 h (at 100 cd/m^2) and an impressive J_{90} of 95.58 mA/cm^2. Our findings demonstrate the applicability of our single monolayer oriented-CQW LED architecture to fabricate high-performance all-solution processed flexible, and large-area CQW-LEDs.

In this work, we target the proof-of-concept demonstration of these CQW-LEDs using the self-assembly method. However, here, we focused on investigating the effects of all-face-down film of CQWs. For future work, we recommend using the film of CQWs in an edge-up configuration. This film could provide a polarized emission due to the nature of CQWs; the IP emission is highly polarized [66]. In addition, the ligand's population on the edges is lower than that on the surfaces because they are less swollen on the edges. The charge injection from the carrier injection layers to this film would be more efficient than that in face-down and spin-coated films, and additionally the edge-up oriented NPLs establish a much denser packing.

Another suggestion for future work is the investigation of the various combination of face-down and edge-up and different NPLs. For example, the multilayer of face-down film or multilayer combinations of face-down and edge-up film or multilayers of the same or different CQWs could be of great interest to be investigated because the thin film of various CQWs dissolved in the same solvent with the conventional spin-coating method is impossible.

BIBLIOGRAPHY

[1] A. Dong, *et al.*, "Binary nanocrystal superlattice membranes self-assembled at the liquid-air interface," *Nature*, vol. 466, no. 7305, pp. 474–477, 2010.

[2] B. T. Diroll, *et al.*, "Smectic nanorod superlattices assembled on liquid subphases: Structure, orientation, defects, and optical polarization," *Chem. Mater.*, vol. 27, no. 8, pp. 2998–3008, 2015.

[3] M. I. Bodnarchuk, *et al.*, "Host-guest chemistry for tuning colloidal solubility, self-organization and photoconductivity of inorganic-capped nanocrystals," *Nat. Commun.*, vol. 6, 2015.

[4] M. V. Kovalenko and M. I. Bodnarchuk, "Lead halide perovskite nanocrystals: From discovery to self-assembly and applications," *Chimia (Aarau).*, vol. 71, no. 7–8, pp. 461–470, 2017.

[5] E. Hecht, *Hecht_ OPTICS 5th edition*. 2016.

[6] J. Lin *et al.*, "High-Performance Quantum-Dot Light-Emitting Diodes Using NiOx Hole-Injection Layers with a High and Stable Work Function," *Adv. Funct.*

Mater., vol. 30, no. 5, 2020.

[7] H. Zhang, *et al.*, "Quantum-dot and organic hybrid tandem light-emitting diodes with multi-functionality of full-color-tunability and white-light-emission," *Nat. Commun.*, vol. 11, no. 1, 2020.

[8] W. K. Bae *et al.*, "Controlling the influence of Auger recombination on the performance of quantum-dot light-emitting diodes," *Nat. Commun.*, vol. 4, 2013.

[9] Z. Li *et al.*, "Efficient and long-life green light-emitting diodes comprising tridentate thiol capped quantum dots," *Laser Photonics Rev.*, vol. 11, no. 1, p. 1600227, 2017.

[10] B. Liu *et al.*, "Record High External Quantum Efficiency of 19.2% Achieved in Light-Emitting Diodes of Colloidal Quantum Wells Enabled by Hot-Injection Shell Growth," *Adv. Mater.*, vol. 32, no. 8, 2020.

[11] S. Delikanli, *et al.*, "Ultralow Threshold Optical Gain Enabled by Quantum Rings of Inverted Type-I CdS/CdSe Core/Crown Nanoplatelets in the Blue," *Adv. Opt. Mater.*, vol. 9, no. 8, pp. 1–6, 2021.

[12] J. Maskoun *et al.*, "Optical Microfluidic Waveguides and Solution Lasers of Colloidal Semiconductor Quantum Wells," *Adv. Mater.*, vol. 33, no. 10, pp. 1–6, 2021.

[13] W. Brütting, *et al.*, "Device physics of organic light-emitting diodes based on molecular materials," *Org. Electron.*, vol. 2, no. 1, pp. 1–36, 2001.

[14] U. Giovanella *et al.*, "Efficient Solution-Processed Nanoplatelet-Based Light-Emitting Diodes with High Operational Stability in Air," *Nano Lett.*, vol. 18, no.

6, pp. 3441–3448, 2018.

[15] B. Liu *et al.*, “Nanocrystal light-emitting diodes based on type II nanoplatelets,” *Nano Energy*, vol. 47, no. March, pp. 115–122, 2018.

[16] X. Dai *et al.*, “Solution-processed, high-performance light-emitting diodes based on quantum dots,” *Nature*, vol. 515, no. 7525, pp. 96–99, 2014.

[17] A. Antanovich *et al.*, “Self-Assembly of CdSe Nanoplatelets into Stacks of Controlled Size Induced by Ligand Exchange,” *J. Phys. Chem. C*, vol. 120, no. 10, pp. 5764–5775, 2016.

[18] M. A. Boles *et al.*, “Self-assembly of colloidal nanocrystals: From intricate structures to functional materials,” *Chem. Rev.*, vol. 116, no. 18, pp. 11220–11289, 2016.

[19] C. B. Murray *et al.*, “Synthesis and Characterization of Nearly Monodisperse CdE (E = S, Se, Te) Semiconductor Nanocrystallites,” *J. Am. Chem. Soc.*, vol. 115, no. 19, pp. 8706–8715, 1993.

[20] S. Volk *et al.*, “Manipulating Electronic Structure from the Bottom-Up: Colloidal Nanocrystal-Based Semiconductors,” *J. Phys. Chem. Lett.*, vol. 11, no. 21, pp. 9255–9264, 2020.

[21] S. Ithurria and D. V. Talapin, “Colloidal Atomic Layer Deposition (c-ALD) using self-limiting reactions at nanocrystal surface coupled to phase transfer between polar and nonpolar media,” *J. Am. Chem. Soc.*, vol. 134, no. 45, pp. 18585–18590, 2012.

[22] S. Ithurria *et al.*, “Colloidal nanoplatelets with two-dimensional electronic

structure," *Nat. Mater.*, vol. 10, no. 12, pp. 936–941, 2011.

[23] H. Dehghanpour Baruj *et al.*, "Highly-directional, highly-efficient solution-processed light-emitting diodes of all-face-down oriented colloidal quantum wells." https://doi.org/10.48550/arXiv.2201.08733, (in submission)

[24] S. Delikanli *et al.*, "Ultrahigh Green and Red Optical Gain Cross Sections from Solutions of Colloidal Quantum Well Heterostructures," *J. Phys. Chem. Lett.*, vol. 12, no. 9, pp. 2177–2182, 2021.

[25] N. Gheshlaghi *et al.*, "Self-Resonant Microlasers of Colloidal Quantum Wells Constructed by Direct Deep Patterning," *Nano Lett.*, vol. 21, no. 11, pp. 4598–4605, 2021.

[26] Y. Shirasaki et al., "Emergence of colloidal quantum-dot light-emitting technologies," *Nat. Photonics*, vol. 7, no. 1, pp. 13–23, 2013.

[27] M. Pelton, "Carrier Dynamics, Optical Gain, and Lasing with Colloidal Quantum Wells," *J. Phys. Chem. C*, vol. 122, no. 20, pp. 10659–10674, 2018.

[28] Y. Kelestemur et al., "Colloidal CdSe Quantum Wells with Graded Shell Composition for Low-Threshold Amplified Spontaneous Emission and Highly Efficient Electroluminescence," *ACS Nano*, vol. 13, no. 12, pp. 13899–13909, 2019.

[29] A. Polovitsyn *et al.*, "Synthesis of Air-Stable CdSe/ZnS Core-Shell Nanoplatelets with Tunable Emission Wavelength," *Chem. Mater.*, vol. 29, no. 13, pp. 5671–5680, 2017.

[30] S. Shendre *et al.*, "Ultrahigh-efficiency aqueous flat nanocrystals of

CdSe/CdS@Cd1−xZnxS colloidal core/crown@alloyed-shell quantum wells," *Nanoscale*, vol. 11, no. 1, pp. 301–310, 2019.

[31] Z. Chen et al., "Quasi-2D colloidal semiconductor nanoplatelets for narrow electroluminescence," *Adv. Funct. Mater.*, vol. 24, no. 3, pp. 295–302, 2014.

[32] E. Lhuillier et al., "Two-Dimensional colloidal metal chalcogenides semiconductors: Synthesis, spectroscopy, and applications," *Acc. Chem. Res.*, vol. 48, no. 1, pp. 22–30, Jan. 2015.

[33] A. G. Vitukhnovsky, et al., "Electroluminescence from colloidal semiconductor CdSe nanoplatelets in hybrid organic-inorganic light emitting diode," *Chem. Phys. Lett.*, vol. 619, pp. 185–188, 2015.

[34] A. A. Rossinelli *et al.*, "Compositional Grading for Efficient and Narrowband Emission in CdSe-Based Core/Shell Nanoplatelets," *Chem. Mater.*, vol. 31, no. 22, pp. 9567–9578, 2019.

[35] M. Sharma, et al., "Two-Dimensional CdSe-Based Nanoplatelets: Their Heterostructures, Doping, Photophysical Properties, and Applications," *Proc. IEEE*, vol. 108, no. 5, pp. 655–675, 2020.

[36] S. Nowy et al., "Light extraction and optical loss mechanisms in organic light-emitting diodes: Influence of the emitter quantum efficiency," *J. Appl. Phys.*, vol. 104, no. 12, 2008.

[37] J. A. Schuller *et al.*, "Orientation of luminescent excitons in layered nanomaterials," *Nat. Nanotechnol.*, vol. 8, no. 4, pp. 271–276, 2013.

[38] R. Scott *et al.*, "Directed emission of CdSe nanoplatelets originating from

strongly anisotropic 2D electronic structure," *Nat. Nanotechnol.*, vol. 12, no. 12, pp. 1155–1160, 2017.

[39] M. Sharma *et al.*, "Near-Unity Emitting Copper-Doped Colloidal Semiconductor Quantum Wells for Luminescent Solar Concentrators," *Adv. Mater.*, vol. 29, no. 30, pp. 1–10, 2017.

[40] J. Heckmann *et al.*, "Directed Two-Photon Absorption in CdSe Nanoplatelets Revealed by k-Space Spectroscopy," *Nano Lett.*, vol. 17, no. 10, pp. 6321–6329, 2017.

[41] Y. Gao et al., "CdSe Nanoplatelet Films with Controlled Orientation of their Transition Dipole Moment," *Nano Lett.*, vol. 17, no. 6, pp. 3837–3843, 2017.

[42] A. W. Achtstein, et al., "Linear Absorption in CdSe Nanoplates: Thickness and Lateral Size Dependency of the Intrinsic Absorption," *J. Phys. Chem. C*, vol. 119, no. 34, pp. 20156–20161, 2015.

[43] A. B. Vasista, et al., "Fourier Plane Optical Microscopy and Spectroscopy," *Digit. Encycl. Appl. Phys.*, pp. 1–14, 2019.

[44] X. Chen, et al., "Angular distribution of polarized light and its effect on light extraction efficiency in AlGaN deep-ultraviolet light-emitting diodes," *Opt. Express*, vol. 24, no. 10, p. A935, 2016.

[45] M. A. Lieb, et al., "Single-molecule orientations determined by direct emission pattern imaging," *J. Opt. Soc. Am. B*, vol. 21, no. 6, p. 1210, 2004.

[46] H. Budde *et al.*, "Raman Radiation Patterns of Graphene," *ACS Nano*, vol. 10, no. 2, pp. 1756–1763, 2016.

[47] Q. Yuan, et al., “A review on the electroluminescence properties of quantum-dot light-emitting diodes,” *Org. Electron.*, vol. 90, no. January, p. 106086, 2021.

[48] H. Shen, et al., “High-efficiency, Low turn-on voltage blue-violet quantum-dot-based light-emitting diodes,” *Nano Lett.*, vol. 15, no. 2, pp. 1211–1216, 2015.

[49] J. Song *et al.*, “Over 30% External Quantum Efficiency Light-Emitting Diodes by Engineering Quantum Dot-Assisted Energy Level Match for Hole Transport Layer,” *Adv. Funct. Mater.*, vol. 29, no. 33, 2019.

[50] C. Pu *et al.*, “Electrochemically-stable ligands bridge the photoluminescence-electroluminescence gap of quantum dots,” *Nat. Commun.*, vol. 11, no. 1, pp. 1–10, 2020.

[51] S. Delikanli *et al.*, “Continuously Tunable Emission in Inverted Type-I CdS/CdSe Core/Crown Semiconductor Nanoplatelets,” *Adv. Funct. Mater.*, vol. 25, no. 27, pp. 4282–4289, 2015.

[52] F. Shabani *et al.*, “Deep-Red-Emitting Colloidal Quantum Well Light-Emitting Diodes Enabled through a Complex Design of Core/Crown/Double Shell Heterostructure,” *Small*, vol. 2106115, p. 2106115, 2021.

[53] S. Delikanli, et al., “Ultralow Threshold Optical Gain Enabled by Quantum Rings of Inverted Type-I CdS/CdSe Core/Crown Nanoplatelets in the Blue,” *Adv. Opt. Mater.*, vol. 9, no. 8, 2021.

[54] Y. Altintas *et al.*, “Giant Alloyed Hot Injection Shells Enable Ultralow Optical Gain Threshold in Colloidal Quantum Wells,” *ACS Nano*, vol. 13, no. 9, pp. 10662–10670, 2019.

[55] A. A. Rossinelli et al., “High-temperature growth of thick-shell CdSe/CdS core/shell nanoplatelets,” *Chem. Commun.*, vol. 53, no. 71, pp. 9938–9941, 2017.

[56] Y. Altintas *et al.*, “Highly Stable, Near-Unity Efficiency Atomically Flat Semiconductor Nanocrystals of CdSe/ZnS Hetero-Nanoplatelets Enabled by ZnS-Shell Hot-Injection Growth,” *Small*, vol. 15, no. 8, 2019.

[57] L. Korala and A. L. Prieto, “Chemical Functionalization of Colloidal Inorganic Nanocrystals (NCs) via Ligand Exchange,” in *Reference Module in Chemistry, Molecular Sciences and Chemical Engineering*, Elsevier, 2017.

[58] O. Erdem *et al.*, “Orientation-Controlled Nonradiative Energy Transfer to Colloidal Nanoplatelets: Engineering Dipole Orientation Factor,” *Nano Lett.*, vol. 19, no. 7, pp. 4297–4305, 2019.

[59] B. Abécassis et al., “Self-assembly of CdSe nanoplatelets into giant micrometer-scale needles emitting polarized light,” *Nano Lett.*, vol. 14, no. 2, pp. 710–715, 2014.

[60] M. Wu, M. I. Bodnarchuk et al., “Large-Area Ordered Superlattices from,” *ACS Nano*, vol. 4, no. 1, pp. 423–431, 2010.

[61] M. A. Boles and D. V Talapin, “Self-assembly of tetrahedral cdse nanocrystals: Effective ‘patchiness’ via anisotropic steric interaction,” *J. Am. Chem. Soc.*, vol. 136, no. 16, pp. 5868–5871, 2014.

[62] Gerrard et al., “Nphoton.2007.34.Zheludev.Comm.Indd,” vol. 1, no. April, pp. 1–4, 2007.

[63] H. V. Demir et al., “Quantum dot integrated LEDs using photonic and excitonic

color conversion," *Nano Today*, vol. 6, no. 6. Elsevier Ltd, pp. 632–647, 2011.

[64] F. Zhang *et al.*, "Super color purity green quantum dot light-emitting diodes fabricated by using CdSe/CdS nanoplatelets," *Nanoscale*, vol. 8, no. 24, pp. 12182–12188, 2016.

[65] X. Dai *et al.*, "Solution-processed, high-performance light-emitting diodes based on quantum dots," *Nature*, vol. 515, no. 7525, pp. 96–99, 2014.

[66] J. M. Pietryga *et al.*, "Spectroscopic and device aspects of nanocrystal quantum dots," *Chem. Rev.*, vol. 116, no. 18, pp. 10513–10622, 2016.

[67] Y. Sun et al., "Efficient quantum dot light-emitting diodes with a Zn0.85Mg0.15O interfacial modification layer," *Nanoscale*, vol. 9, no. 26, pp. 8962–8969, 2017.

[68] L. Qian et al., "Stable and efficient quantum-dot light-emitting diodes based on solution-processed multilayer structures," 2011.

[69] A. Chutinan et al., "Theoretical analysis on light-extraction efficiency of organic light-emitting diodes using FDTD and mode-expansion methods," *Org. Electron.*, vol. 6, no. 1, pp. 3–9, 2005.

[70] G. H. V. Bertrand et al., "Shape control of zincblende CdSe nanoplatelets," *Chem. Commun.*, vol. 52, no. 80, pp. 11975–11978, Sep. 2016.

[71] H. Shen et al., "High-Efficiency, Low Turn-on Voltage Blue-Violet Quantum-Dot-Based Light-Emitting Diodes," *Nano Lett*, vol. 6, p. 57, 2015.

[72] E. M. Miller *et al.*, "Revisiting the Valence and Conduction Band Size

Dependence of PbS Quantum Dot Thin Films," *ACS Nano*, vol. 10, no. 3, pp. 3302–3311, 2016.

[73] D. M. Kroupa *et al.*, "Tuning colloidal quantum dot band edge positions through solution-phase surface chemistry modification," *Nat. Commun.*, vol. 8, no. May, pp. 2–9, 2017.

[74] Q. Su, H. Zhang, and S. Chen, "Flexible and tandem quantum-dot light-emitting diodes with individually addressable red/green/blue emission," *npj Flex. Electron.*, vol. 5, no. 1, 2021.